Combined physical and biogeochemical assessment of mesoscale eddy parameterisations in ocean models: eddy induced advection at non-eddying resolutions

X. Ruan[a,b,1], D. Couespel[c,d], M. Lévy[d], J. Li[a,b], J. Mak[a,b,1], Y. Wang[a,b]

[a]*Department of Ocean Science, Hong Kong University of Science and Technology*
[b]*Southern Marine Science and Engineering Guangdong Laboratory (Guangzhou)*
[c]*NORCE Norwegian Research Centre, Bjerknes Centre for Climate Research*
[d]*Sorbonne Université, LOCEAN-IPSL, CNRS/IRD/MNHN*

Abstract

Ocean components of Earth System Models employed for climate projections as yet do not routinely resolve mesoscale eddies for computational cost reasons, and the associated subgrid processes are still parameterised in these numerical models. While the performance of physics parameterisations in a numerical ocean model is normally assessed via examining the associated physical responses, biogeochemical responses are also important, but are often treated separately. Given recent advances in mesoscale eddy parameterisations, specifically for the eddy induced advection, this work systematically examines the improvements brought about by the inclusion of a time and space varying eddy induced velocity coefficient, and examine the joint consequences for physical and biogeochemical responses in the context of an idealised but ocean relevant model. Relative to a high resolution mesoscale eddy resolving model, the more updated mesoscale eddy parameterisation is able to capture aspects of the model truth in the physical responses. However the biogeochemistry response is rather more subtle, where a 'better' response with the conventional eddy parameterisation with a constant coefficient could arise from a physically inconsistent response. The present work provides some baseline model sensitivities from which future assessments employing other parameterisations or in more complex settings could compare against.

Keywords: mesoscale eddy parameterisation, numerical modelling, climate change, biophysical interactions

1. Introduction

The ocean circulation plays a crucial role in the Earth system's heat, carbon and nutrient cycles, with associated effects on the global climate and the marine ecosystem (e.g. Rahmstorf, 2002; Doney et al., 2012). Over the decadal to centennial time-scales, more heat is expected to reside in the upper part of the ocean under climate projection exercises (e.g, IPCC, 2019), which is known to strengthen the upper ocean stratification, leading to changes in the ocean ventilation pathways (e.g., Bindoff and McDougall, 1994; Li et al., 2020). The ocean meridional overturning circulation is projected to slow down, partly via the shoaling of the pycnocline, though uncertainties still exist (e.g., Bellomo et al., 2021). Changes in the ocean overturning circulation can affect the bulk transport of nutrients, which can then have large-scale impacts on the phytoplankton populations. Phytoplankton, being primary producers, plays an important role in the global carbon cycle, and impact issues of food security via its role at the base of most oceanic food webs. While there is large uncertainty in the physiological responses of various marine biomass to the changing marine environment in terms of heat stress, nutrient abundance, acidity and others (e.g., Kwiatkowski et al., 2020; Tagliabue et al., 2021; Martiny et al., 2022), it is not controversial to say there is a clear causal link in how the physical circulation can impact the broad regional and global biogeochemical response via its influence on nutrient

Email addresses: xruanaa@connect.ust.hk (X. Ruan), julian.c.l.mak@googlemail.com (J. Mak)
[1]Corresponding authors.

supply, though such projections often come with large uncertainties given the nonlinear interactions present in the complex Earth system (e.g., Lotze et al., 2019).

An invaluable tool for probing and constraining the physical and biogeochemical responses in the marine system to the changing environment are Earth System Models. These are numerical models that simulate the evolution of the earth system components and their interactions, such as the ocean, the marine ecosystem, and the atmosphere (e.g., Bonan and Doney, 2018; Séférian et al., 2019; Lee et al., 2022), with the assumption that the processes implemented into the numerical models are themselves correct. However, even with the increasing computational power available, present state-of-the-art Earth System Models still mostly utilise ocean components at approximately 1° horizontal resolution, which does not explicitly permit geostrophic mesoscale eddies (e.g., Hewitt et al., 2020, 2022). It is known that geostrophic mesoscale eddies play a crucial role in regulating the ocean circulation response, where such motions not only have local effects, but also on the larger scale regional and global mean state (e.g. Lévy et al., 2012). Although there is an increasing push for ocean models to be mesoscale eddy resolving (Fox-Kemper et al., 2019; Kwiatkowski et al., 2020; Hewitt et al., 2022) or at least eddy rich (at around $1/12^\circ$ horizontal resolutions, Hallberg, 2013), global Earth System Models at such resolutions remain computationally prohibitive, and global Earth System Models with an ocean component at the mesoscale eddy permitting regime at around $1/4^\circ$ horizontal resolution is a more realistic target (Hewitt et al., 2017, 2020, 2022; Roberts et al., 2020). Given the important role the ocean plays in the physical and biogeochemical response, and the anticipated developments of ocean models over the next decade, there is a need to probe, constrain and understand the sensitivities of the physical and biogeochemical responses in ocean models at the non-eddy resolving, eddy permitting as well as the eddy rich/resolving resolutions.

For those models that do not explicitly permit mesoscale eddies, parameterisations are often employed to mimic the feedback of geostrophic mesoscale eddies on the modelled state that would be present in an eddy rich/resolving model. Often employed are what we would term here as *diffusive* closures, such as isoneutral diffusion (e.g., Redi, 1982; Griffies, 1998) and the Gent–McWilliams (GM) scheme (Gent and McWilliams, 1990; Gent et al., 1995). Isoneutral diffusion leads to tracer diffusion along the isoneutral directions, while the GM scheme leads to an eddy induced advection of tracers and results in a flattening of isoneutral slopes, both consistent with the adiabatic nature of mesoscale eddies generated by baroclinic instabilities (e.g., Vallis, 2006). Such diffusive closures are designed for coarse resolution models with no explicitly resolved eddies, are considered more standard, and most existing numerical ocean models have variants of such schemes implemented (e.g. MITgcm, Marshall et al. 1997a,b; NEMO, Madec 2008; FESOM, Wang et al. 2014; MOM, Adcroft et al. 2019). On the other hand, mesoscale eddies can also lead to sharpening of large-scale jets (via inverse cascades, eddy induced momentum convergence, or otherwise, e.g. Waterman and Jayne, 2012; Waterman and Hoskins, 2013), which is increasingly modelled by *backscatter* based parameterisations (e.g., Bachman, 2019; Jansen et al., 2019). Both diffusive and backscatter types of schemes have been developed since their respective conceptions, and recent advances in both classes of parameterisations have led to lower resolution models that are more in line with the eddy rich/resolving models, at least in the physical responses. Advances in diffusive schemes tend to focus more on coarse resolution models, some of which have been shown to lead to improvements in sensitivities of the circulation to changing forcing scenarios (e.g., Farneti et al., 2015; Mak et al., 2018, 2022b). Backscatter schemes have received more attention in eddy permitting models, in their ability to strengthen the represented eddy energy levels and ocean currents (e.g., Bachman, 2019; Jansen et al., 2019).

The biogeochemical responses to such recent updates in physics parameterisations has been, on the other hand, somewhat lacking. However, it is well-known that the model represented physics can have very substantial impact on the resulting physical and/or biogeochemical metrics of interest. Modifying the represented eddy-mean feedbacks can have a significant effect on the ventilation rate and pathways, which are expected to lead to significant impacts on the represented ocean heat content (e.g., de Boer et al., 2007; Zhang and Vallis, 2013; Zanna et al., 2019; Mak et al., 2022b; Newsom et al., 2022), carbon (England and Rahmstorf, 1999; Gnanadesikan et al., 2015; Khwatiwala et al., 2018), oxygen (Matear et al., 2000; Helm et al., 2011; Bopp et al., 2017; Takano et al., 2018), and nutrient distributions (Lévy et al., 1999; Tschumi et al., 2011; Bopp et al., 2013; Couespel et al., 2021). Given the prevalent use of numerical ocean general circulation models for probing biophysical interactions and for making predictions (e.g., Bopp et al., 2013; Berthet et al., 2019; Swearer et al., 2019; Séférian et al., 2019), it is important to investigate (*i*) how the physics parameterisations modify the modelled physical states, and (*ii*) how that in turn affects the biogeochemical responses, given there is no guarantee that improvements in physical processes necessarily leads to a 'better' biogeochemical response depending on the metric of choice, given the nonlinear interactions inherent in a complex system.

Global and/or realistic models, while useful for their intended arena of making predictions and informing policies

(e.g., IPBES, 2019), are computationally expensive and possess a large number of degrees of freedom, making them somewhat difficult in attributing the various causalities. While ultimately these realistic and complex Earth System Models should be used when assessing the impacts of eddy parameterisations, for delineating the causality and interactions between the physical parameterisations and the resulting physical and biogeochemical responses, we consider here a complementary approach by utilising idealised numerical models. We focus in this work on a systematic assessment of mesoscale eddy parameterisations and its impact on Net Primary Production (NPP), via the former's influence on the nutrient stream or relay (e.g., Williams et al., 2017, 2011; Whitt and Jansen, 2020; Gupta et al., 2022) in the well-known double gyre setting with a simple biogeochemistry model, and with prescribed atmospheric forcing in a control as well as an idealised climate change scenario following the work of Couespel et al. (2021). The idealised model has the benefit that the physical processes are well-known, and is computationally tractable that high resolution eddy resolving 'model truths' are available.

Even with the reduced complexity afforded by the choice of numerical model, there are multiple parameterisations for mesoscale turbulence currently, and examining the impact of diffusive and backscatter-type approaches on the physical and biogeochemical response together, in a hierarchy of models with different horizontal resolutions with different dynamical regimes, is a gargantuan undertaking. We focus in this first article the impacts on the physical and biogeochemical responses emerging from different diffusive eddy closures, specifically focusing on the GM-based parameterisations for the eddy induced advection. An analogous investigation into the effects of isoneutral diffusion, backscatter type eddy parameterisations, and analogous extensions into the eddy permitting models will be reported in subsequent publications. The models to be investigated here are non-eddy resolving, differing by the GM-type closures they employ, and the performance of these will be judged against the high resolution eddy resolving model truths. The GM parameterisation variants and the numerical model set up are described in §2. In §3 we report the differences in the physical and biogeochemical responses arising from the choice of closures. In §4 we subject the models to idealised climate change scenarios to investigate model sensitivities. The article concludes in §5, critically evaluating the advantages and shortfalls provided by the choices of GM-based closures.

2. Mesoscale eddy parameterisations and numerical set up

Two canonical types of diffusive closures associated with geostrophic turbulence are those based on isoneutral diffusion (e.g., Redi, 1982) and the Gent–McWilliams scheme (GM, Gent and McWilliams, 1990). The former refers to diffusion of tracers along the isoneutral direction, while the latter resembles a horizontal buoyancy diffusion (in the quasi-geostrophic limit, e.g. Treguier et al., 1997) or a layer thickness diffusion (e.g., Gent and McWilliams, 1990), but is really an eddy induced advection (e.g., Gent et al., 1995; Treguier et al., 1997; Griffies, 1998). While it is known that both have effects on the resulting physical and biogeochemical response, we note that while isoneutral diffusion modifies the rate of tracer ventilation, GM schemes affect the structure (and thus the rate) of the tracer ventilation through its impact on the density stratification. It is certainly true there are more studies focusing on assessing GM-based schemes (e.g., Visbeck et al., 1997; Eden and Greatbatch, 2008; Cessi, 2008; Hofman and Morales Maqueda, 2011; Munday et al., 2013; Zhang and Vallis, 2013; Bates et al., 2014; Farneti et al., 2015; Mak et al., 2018, 2022b), although there have also been increasing interest in isoneutral diffusion, assessing its impact as well as improving on the standard implementation with constant diffusivity (e.g., Ferrari and Nikurashin, 2010; Pradal and Gnanadesikan, 2014; Jones and Cessi, 2016; Jones and Abernathey, 2019; Groeskamp et al., 2021; Holmes et al., 2022; Chouksey et al., 2022). Both processes are related to mesoscale turbulence, and works exist suggesting relationships between the two (e.g., Smith and Marshall, 2009; Abernathey et al., 2013). Owing to the larger interest in GM-based closures, in this work we make the choice to focus primarily on the consequences afforded by different GM-based schemes, and consider a prescribed constant isoneutral diffusivity $\kappa_{\rm iso}$. The model sensitivity to $\kappa_{\rm iso}$ by itself is was found to be rather mild in the present model, although nonlinear feedback loops can be present, suggesting that further investigation is required in this area; see Appendix A for details.

2.1. GM-based parameterisations

The GM-scheme introduces an extra eddy induced velocity $\mathbf{u}^* = -\nabla\times(\kappa_{\rm gm}\boldsymbol{s})$ (e.g., Ferreira et al., 2005) to the tracer advection equation, where $\boldsymbol{s} = M^2/N^2$ is the isopycnal slope in the horizontal directions, with $M^2 \sim |\nabla_H\rho|^2$ (where ρ is the relevant density and ∇_H denotes the horizontal gradient operator) and $N^2 \sim -\partial\rho/\partial z$ denoting the horizontal and

vertical buoyancy gradients associated with the resolved state, and $\kappa_{\rm gm}$ will be termed the GM-coefficient in this work. The GM scheme is widely used because of its inherent properties, such as adiabatic advection leading to slumping of isopycnals, positive-definite generation of eddy energy, layer-wise conservation of moments; e.g., (Gent et al., 1995), as well as numerical advantages that it can impart to a model (numerical stability due to the slumping action, reduction of unrealistic deep convection; e.g., Danabasoglu et al. 1994). A choice often utilised in idealised models takes the simple prescription of

$$\kappa_{\rm gm} = \kappa_0 = \text{constant}. \tag{1}$$

2.1.1. GEOMETRIC

It is widely acknowledged that it is desirable to maintain the properties afforded by the GM scheme even if one does not believe a simple prescription of $\kappa_{\rm gm}$ = constant will suffice. A prevalent research focus has thus been on improving on the functional form of $\kappa_{\rm gm}$ (e.g., Visbeck et al., 1997; Treguier et al., 1997; Ferreira et al., 2005; Cessi, 2008; Eden and Greatbatch, 2008; Hofman and Morales Maqueda, 2011; Marshall et al., 2012; Jansen et al., 2015). The focus here will be on the GEOMETRIC prescription of the $\kappa_{\rm gm}$ (Marshall et al., 2012; Mak et al., 2018, 2022b), which takes

$$\kappa_{\rm gm} = \alpha \frac{\int E \, \mathrm{d}z}{\int (M^2/N) \, \mathrm{d}z}, \tag{2}$$

where α is a non-dimensional tuning parameter (bounded in magnitude by 1), E is the total (potential and kinetic) eddy energy, and the resulting $\kappa_{\rm gm}$ varies in time and the horizontal (but is depth-independent with the present specification). The prescription allows a more significant state-dependent response. Unlike most other existing proposals for the $\kappa_{\rm gm}$ that utilise mixing length type arguments with dependence on the eddy kinetic energy, the GM-version of GEOMETRIC arises from a mathematically rigorous bound that results from analysing the Eliassen–Palm flux tensor that encodes the eddy-mean feedbacks (Marshall et al., 2012; Maddison and Marshall, 2013). Notably, out of the GM-based proposals, the GM-version of GEOMETRIC has somewhat more evidence in support of its use, from a diagnostic point of view (Bachman et al., 2017; Wang and Stewart, 2020; Wei et al., 2022), and prognostic calculations in idealised models (Mak et al., 2017, 2018) as well as in realistic models (Mak et al., 2022b). In particular, the GM-version of GEOMETRIC in the aforementioned prognostic calculations have been shown to lead to improved sensitivities of the modelled ocean circulation (notably the Antarctic Circumpolar Current transport and the global Meridional Overturning Circulation strength) to changes in forcing over standard prescriptions of the $\kappa_{\rm gm}$.

In a prognostic calculation with a coarse resolution model, E is provided by means of a depth-integrated eddy energy budget. Denoting (x, y) to be the zonal and meridional directions respectively, following Mak et al. (2022b), the eddy energy budget is given by

$$\frac{\mathrm{d}}{\mathrm{d}t}\int E \, \mathrm{d}z + \underbrace{\nabla_H \cdot \left((\widetilde{\mathbf{u}}^z - |c| \, \mathbf{e}_x) \int E \, \mathrm{d}z \right)}_{\text{advection}} = \underbrace{\int \kappa_{\rm gm} \frac{M^4}{N^2} \, \mathrm{d}z}_{\text{source}} - \underbrace{\lambda \int (E - E_0) \, \mathrm{d}z}_{\text{dissipation}} + \underbrace{\eta_E \nabla_H^2 \int E \, \mathrm{d}z}_{\text{diffusion}}, \tag{3}$$

where the depth-integrated eddy energy is advected by the depth average flow $\widetilde{\mathbf{u}}^z$ with westward propagation at the long Rossby wave phase speed $|c|$ (e.g., Chelton et al., 2011; Klocker and Marshall, 2014). The growth of eddy energy comes from slumping of mean density surfaces, and energy diffused in the horizontal (Grooms, 2015; Ni et al., 2020a,b), with ∇_H denoting the horizontal gradient operator and the η_E the associated eddy energy diffusivity. A linear dissipation of eddy energy at rate λ (but maintaining a minimum eddy energy level E_0) is utilized, so λ^{-1} is an eddy energy dissipation time-scale.

In this work we focus on the GM-version of the GEOMETRIC parameterisation, choosing the standard constant $\kappa_{\rm gm}$ as a 'worse case scenario' setting. We provide some discussion based on results utilising simpler proposals of spatially $\kappa_{\rm gm}$ (Treguier et al. 1997; cf. Visbeck et al. 1997) as well as speculate on the responses that might be expected when utilising other existing energetically constrained proposals (e.g., $\kappa_{\rm gm} \sim \sqrt{K}$ of Jansen et al., 2019, where K is the eddy kinetic energy) based on the results of this work in the discussion section.

2.2. Model set up

To isolate and identify influences arising from the parameterisation variants, an idealised numerical ocean model is used. While there are many possible choices, we note that the previous investigation of Couespel et al. (2021) utilise

a double gyre model with the Nucleus for European Modelling of the Ocean (NEMO; Madec 2008). The particular gyre model in Couespel et al. (2021) is a "straightened" version of the standard gyre configuration test case that comes with NEMO, which is already coupled to an idealised biogeochemistry model within NEMO (cf. Lévy et al., 2010, 2012), and has been used to study both physical and biogeochemical responses in the aforementioned works.

To leverage and compare with the results from existing works, we will essentially be employing the same model and set up from Couespel et al. (2021), albeit with mild differences, to investigate the response of physical and biogeochemical responses to the GM-based mesoscale eddy parameterisations. To recap, the physical model employed by Couespel et al. (2021) is on a square domain with sides of length 3180 km and depth 4 km, formulated on a β-plane centred around 35° N. The domain has no bathymetry, is bounded by vertical walls that are aligned with longitudes and latitudes on all sides, and with non-linear bottom drag and free slip condition on the lateral boundaries. The model utilises a linear equation of state with temperature and salinity, and vertical mixing is via a turbulent kinetic energy scheme which comes standard with NEMO (Gaspar et al., 1990). Atmospheric forcing is through the flux formulation, and the forcings (wind stress, penetrative solar radiation, pesudo-atmospheric temperature Θ^* for computing sea surface temperature restoring, freshwater flux) are all zonally symmetric and with a prescribed seasonal cycle, and there is no net salinity flux (see Lévy et al., 2010, Fig.1). The model employs the same idealised biogeochemistry model LOBSTER (see e.g., Lévy et al., 2012), with standard reference settings, and the passive tracer advection and diffusion uses the active tracer settings. The LOBSTER model uses nitrogen as the currency, and the six variables are concentrations of detritus, zooplankton, phytoplankton, nitrate, ammonium, and dissolved organic matter; variables of particular interest to the work here are phytoplankton and nitrate for their links to Net Primary Production (NPP). Note that LOBSTER does not represent physiological changes with changes in temperature, so changes that are observed will be solely due to changes in the transport, which is in line with our focus on the large-scale links between physics and biogeochemistry.

The differences in the model employed in this work to that of Couespel et al. (2021) are the following:

- version of NEMO (NEMO v4.0.5 r14538 instead of v3.4 r4826),
- a slightly different initialisation of nitrate concentration at the beginning of the spinup (from version differences), and at the start of the perturbation experiments (no averaging of the deep ocean nitrate concentration),
- the model truth is taken here to have a horizontal resolution of $1/12°$ instead of $1/9°$.

Part of the reason for the more updated version of NEMO is for its implementation of a GM-version of GEOMETRIC from the work of Mak et al. (2022b), and it was easier to adapt the model configuration to the newer NEMO than to write the GEOMETRIC parameterisation into an older version of NEMO. Sample calculations show that the different choices of initialisation of the nitrate concentration at the deeper ocean have essentially no impact on the conclusions in this article. The horizontal resolution of the model truth was increased in this work partly as a balance to resolve the mesoscales, but without resolving too much of the submesoscales, given the main focus here on mesoscale dynamics. Another reason for taking the model truth to be $1/12°$ is for the suggestive analogy with the global NEMO ORCA0083 (sometimes known as ORCA12) configuration at a nominally horizontal resolution of $1/12°$, with our aim to consider the effect of parameterisations on physical and biogeochemical response in a future work using a hierarchy of idealised models at at the eddy permitting regime with models at intermediate resolutions. All the major conclusions of Couespel et al. (2021) are found to hold here, up to minor and inconsequential quantitative differences.

A summary of key model parameters are given in Table 1, partly informed by previous works (Couespel et al., 2021; Mak et al., 2022b,a); a brief description of model sensitivities to some of these choices are given in Appendix A. Following the strategy of Couespel et al. (2021), the physical and biogeochemical model at the 1° resolution starts from model year −2300, spun up over 2000 model years to model year −300 using the CONST variant with constant κ_{gm}. At model year −300, perturbation experiments were carried out for another 300 years to model year 0 (which is longer than the 100 years considered in Couespel et al. 2021). For the 1° models, the perturbation experiments are with CONST and GEOM. For the $1/12°$ model, the fields are simply interpolated from the 1° model onto the $1/12°$ grid. Fig. 1 shows some of the summary statistics of the spinup, indicating a quasi-equilibrium has been reached at least in the upper parts of the ocean (depths less than 700 m), and in line with the results of Couespel et al. (2021)

	R1 (CONST and GEOM)	R12
horizontal resolution	106 km	8.83 km
time step	30 mins	10 mins
momentum diffusion	horizontal ∇^2, $\nu = 10^5$ m s^{-2}	horizontal ∇^4, $\nu = -3 \times 10^{10}$ m s^{-4}
tracer advection	FCT scheme	MUSCL scheme
tracer diffusion	isopycnal ∇^2, $\kappa_{\rm iso} = 10^3$ m s^{-2}	iso-level ∇^4, $\kappa = -10^9$ m s^{-4}
eddy induced advection	CONST ($\kappa_{\rm gm} = 1000$ m s^{-1})	—
	GEOM ($\alpha = 0.04$, $\lambda^{-1} = 135$ days)	—

Table 1: Key model parameter differences between the calculations considered in this work.

(see their Fig. 1*c* and A1). A working hypothesis is that the physical and biogeochemical responses are improved in the GEOM calculations when compared to the CONST calculations; the eventual supporting evidence suggests this is largely true (see Table 2 in §5), but there are important subtle details to be detailed.

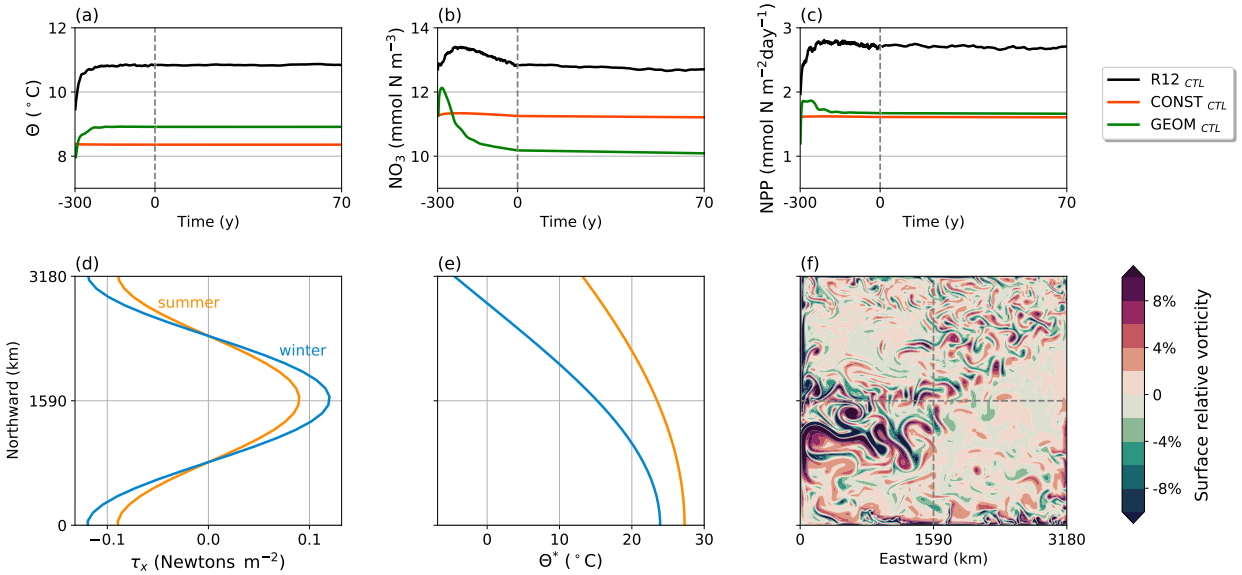

Figure 1: (Top row) Time series of various quantities from the 300-year spin-up (i.e. model years −300 to 0 years) and the experimental period (0 to 70 years), for the model truth (R12, black line) and coarse resolution calculations (CONST, red line; GEOM, green line); the time axes are linear in the spinup and analysis period individually. (*a*) Averaged ocean temperature Θ (°C) over the top 700 m of the model domain. (*b*) Model nitrate concentration (NO3, mmol N m^{-3}, where N is the nitrogen currency unit) over the top 700 m of the model domain. (*c*) Domain integrated Net Primary Production (NPP, mmol N m^{-2} day). Shown also are (*d*) the idealised purely zonal wind stress forcing τ_x (Newtons m^{-2}) with seasonal cycle limits, (*e*) the pseudo-atmospheric temperature Θ^* (°C) with seasonal cycle limits, and (*f*) a snapshot of the surface relative vorticity of the model truth R12 (units of the planetary vorticity f_0).

3. Comparison of pre-industrial controls

We first investigate the characteristics displayed by the coarse resolution 1° models and the relative differences with the model truth at 1/12° resolution, with a focus on the GEOM calculations. Each model is integrated for another 70 years from model year 0, subject to the same idealised atmospheric forcing. The diagnostics reported are from data time averaged over the analysis period, taken to be the last five years of the calculation (between start of model year

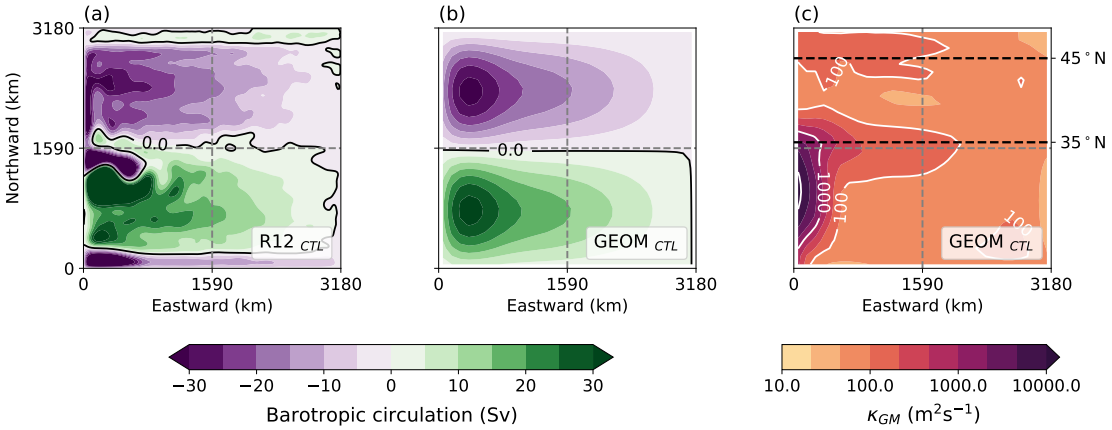

Figure 2: The barotropic streamfunction Ψ_{baro} (in Sv = 10^6 m^3 s^{-1}) of (*a*) R12 and (*b*) GEOM, with the zero contour overlaid as a black line; CONST visually looks identical to GEOM, and has been omitted. Panel (*c*) shows the resulting κ_{gm} distribution from GEOM with the choice of parameters in Table 1.

66 and end of model year 70). Time-averaged quantities are denoted by an overbar

$$\overline{(\cdot)} = \frac{1}{t_1 - t_0} \int_{t_0}^{t_1} (\cdot)\, \mathrm{d}t, \tag{4}$$

with $t_{0,1}$ being start and end of model years 66 and 70 respectively. We first focus on the physical responses before analysing the biogeochemical responses, with a focus on the nutrient supply and its effect on Net Primary Production (NPP). Following the previous work of Couespel et al. (2021), our focus will be on the responses particularly within the subpolar gyre region, which is the area that is most bioactive in the present setup. We employ the same pre-defined box utilised in Couespel et al. (2021) for our analysis, defined as the area bounded by $y = 35°$ N and 45° N, with the boundaries marked on by the black dashed lines in the subsequent figures where appropriate.

3.1. Physical responses

Fig. 2(*a*, *b*) shows the barotropic streamfunction (where the tilde denotes a dummy integration variable)

$$\Psi_{\text{baro}} = \int_{-H}^{0} \int_{0}^{x} \overline{v}(\tilde{x}, y, z)\, \mathrm{d}\tilde{x}\, \mathrm{d}z \tag{5}$$

for the R12 and GEOM calculation; the CONST one has been omitted since visually it is indistinguishable from the GEOM one. Both models display the familiar northern hemisphere double gyre pattern with a subtropical gyre to the south and a subpolar gyre to the north. In the R12 calculation, because of eddy rectification effects, relatively strong re-circulation regions exists near the northern and southern boundaries as Fofonoff gyres (e.g., Berloff, 2005; Marshall and Adcroft, 2010), and the modelled Western Boundary Current is slightly south of the latitudinal center line, even though the zonal wind stress is symmetric about the same center line (cf. Lévy et al., 2010).

In Fig. 2(*c*) we show the resulting $\kappa_{\text{gm}} = \kappa_{\text{gm}}(x, y)$ from GEOM. Note that κ_{gm} is large (on the order of a few thousand) on the Western Boundary Current in the subtropical gyre. On the other hand, the values of κ_{gm} are generally rather small elsewhere in the domain, on the order of a hundred or so. The small values of κ_{gm} away from the Western Boundary Currents arise from the rather weak geostrophic flow present in the gyre system, which by thermal wind shear relation corresponds to weak isopycnal slopes M^2/N^2. The much smaller values of κ_{gm} within the subpolar gyre and particularly its values near the northern boundary will turn out to be an important focus point later on. The resulting domain-averaged value of κ_{gm} is about 300 m^2 s^{-1}, and it is found that models using such a small value of κ_{gm} everywhere introduces un-physical deep convection events particularly along the Western Boundary Current (not

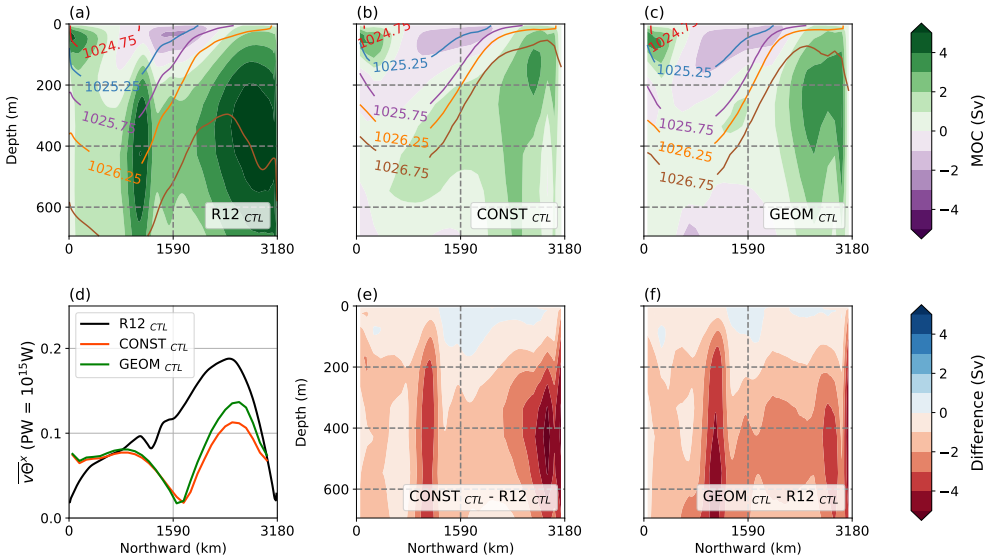

Figure 3: (Top row) The diagnosed Meridional Overturning Circulation streamfunction Ψ_{MOC} from the model (shading, in Sv = 10^6 m^3 s^{-1}) and lines of constant potential density referenced to sea level (contours, in kg m^{-3}), for (*a*) R12, (*b*) CONST, and (*c*) for GEOM. Panel (*d*) shows the diagnosed northward heat transport (in units of PW = 10^{15} W) for all three cases. Panels (*e*, *f*) show the raw differences of the diagnosed Ψ_{MOC} from the coarse resolution models relative to the model truth R12, where red colours denote more negative values, mostly corresponding to a decrease in the overturning strength.

shown; cf. Danabasoglu et al., 1994). One benefit then with parameterisation schemes that allow spatial variations of κ_{gm} is that κ_{gm} is large only where it needs to be large, which is a point that will be revisited throughout the article.

The concentrated signal of κ_{gm} on the Western Boundary observed in Fig. 2(*c*) is also consistent with the fact the explicitly represented Western Boundary Current in a coarse resolution model is rather weak, which would be suggestive that the resulting Meridional Overturning Circulation in the system is also on the weak side. In Fig. 3 we show the diagnosed Meridional Overturning Circulation streamfunction

$$\Psi_{\mathrm{MOC}} = \int_{-H}^{z} \int_{0}^{L_x} \overline{v}(x, y, \tilde{z})\, \mathrm{d}x\, \mathrm{d}\tilde{z} \tag{6}$$

between different calculations, some sample isopycnals using potential density referenced to sea level, as well as the diagnosed depth integrated and zonal-mean northward heat transport $\overline{v\Theta}^{x}$. As can be seen in Fig. 3, the coarse resolution models CONST and GEOM in general have a weaker overturning strength, partially because of a weaker modelled Western Boundary Current arising from the more diffuse nature of the model, and a lack of representation with eddy rectification effects (e.g., Lévy et al., 2010; Waterman et al., 2011; Waterman and Lilly, 2015). The particularly weak overturning in the subtropical region of the coarse resolution models compared to the model truth is consistent with a weak deep Western Boundary Current, related to the structure of the displayed isopycnals via thermal wind shear relation. The weaker overturning is reflected in the weaker northward transport of heat. The use of GEOMETRIC provides mild improvements to the represented overturning strength particularly in the subpolar gyre, where the diagnosed Ψ_{MOC} in GEOM is stronger than that in CONST and closer to R12 (area-weighted average root-mean-square mismatch to R12 of 2.03 Sv in GEOM compared to 2.34 Sv in CONST, calculated north of the center of the domain), coinciding with a larger heat transport (area-weighted average heat transport of 0.094 PW in GEOM compared to 0.078 PW in CONST, calculated from north of the center of the domain). This increased overturning strength is expected to have a positive effect on the modelled biogeochemical response in the GEOM calculation, as we might expect increased nutrient transport into the subpolar gyre by the nutrient stream or relay (e.g., Williams et al., 2017, 2011; Whitt and Jansen, 2020; Gupta et al., 2022).

The double gyre configuration here is such that the downwelling is most prominent in the northern part of the

domain since this region is exposed to the coolest atmospheric temperatures, as seen in the maximum mixed layer depths (diagnosed as the first depth below which $|\sigma_\theta(z) - \sigma_\theta(z = -10\text{ m})| > 0.01$, where σ_θ is the potential density referenced to sea level), shown in Fig. 4(*a-c*). The biggest differences between the calculations are again in the subpolar gyre region, particularly in the northwestern corner of the domain. Fig. 4(*d-f*) shows the histogram of the diagnosed mixed layer north of the subpolar region, and we can see that R12 and GEOM are comparable in their mixed layer depth distributions statistically, while CONST has a notable skew towards shallower mixed layer depths (in terms of median and distribution). The more shallow mixed layer depths observed in the coarse resolution models are consistent with the decrease in the overturning strength, since the mixed layer is correlated to the depth of deep water extent as well as to the depth of the overturning circulation. One rationalisation for the shallower mixed layer depths in CONST compared to GEOM would be the magnitude of κ_{gm} at the northern boundary region region (cf. Fig. 2*c*). The GM scheme acts to flatten isopycnals, and the extra 'resistance' provided by the GM scheme below the base of the mixed layer works against the steepening of isopycnals associated with deep water formation and subsequent convective events. For a similar configuration in the isopycnal slopes, the CONST scheme has a higher κ_{gm} value in the northern boundary region, which leads to more 'resistance' to formation of deeper mixed layers compared to the GEOM case. The causality highlights the importance of the magnitude and distribution of κ_{gm} in the modelled physical mean state of coarse resolution models, where the mean transport pathways and strengths are being influenced by the explicit or parameterised small-scale feedbacks.

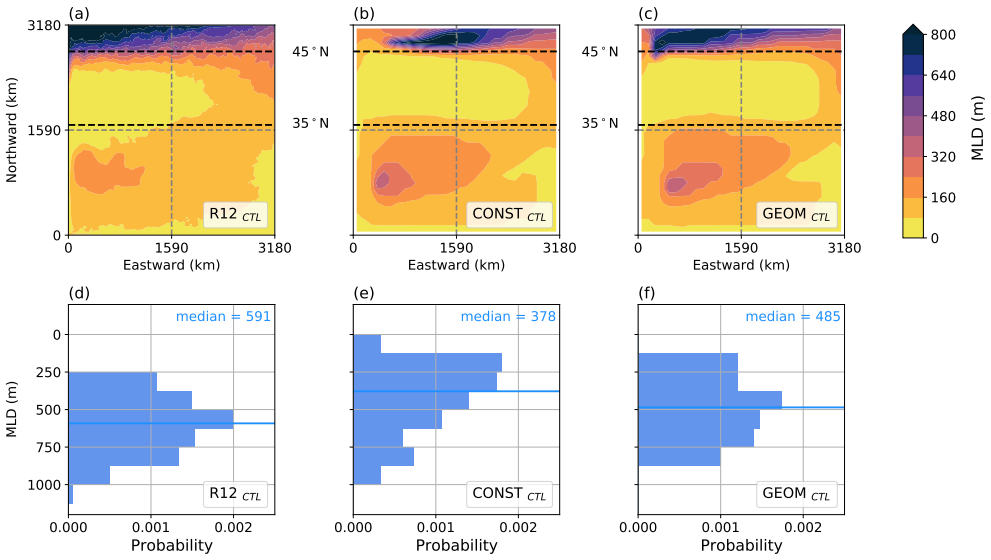

Figure 4: (Top row) Maximum mixed layer depth (m, diagnosed as the first depth below which $|\sigma_\theta(z) - \sigma_\theta(z = -10\text{ m})| > 0.01$, where σ_θ is the potential density referenced to sea level), for (*a*) R12, (*b*) CONST and (*c*) GEOM. (Bottom row) histogram of mixed layer depth distributions and median (marked on as a line) north of the subpolar gyre region, for (*d*) R12, (*e*) CONST and (*f*) GEOM.

3.2. Biogeochemical responses

Since the CONST calculation is expected to have a somewhat weaker circulation given the stronger decline in the overturning in Fig. 3 as well as the shallower mixed layer depths in Fig. 4 compared to the GEOM case, we might expect that GEOM offers some improvements over CONST in the biogeochemical response via changes in the nutrient transport. Fig. 5 shows the vertically integrated NPP as a map over the domain. Note that the CONST calculation has a noticeably smaller signal of NPP in the western boundary in the subpolar gyre region compared to the R12 calculation, but is something that GEOM is able to somewhat capture. In terms of numerical values of the integrated NPP averaged over the subpolar gyre region (units of mmol N m^{-2} day^{-1}, where N is the nitrogen currency), R12 has the largest NPP at 3.67, with CONST at 2.76 and GEOM at 2.91 (respectively a decrease of −24.8% and −20.6% relative to R12). The GEOM calculation results in a modelled state that has closer NPP values to the model truth

R12 compared to the CONST calculation consistent with our expectations, although the improvements are somewhat modest.

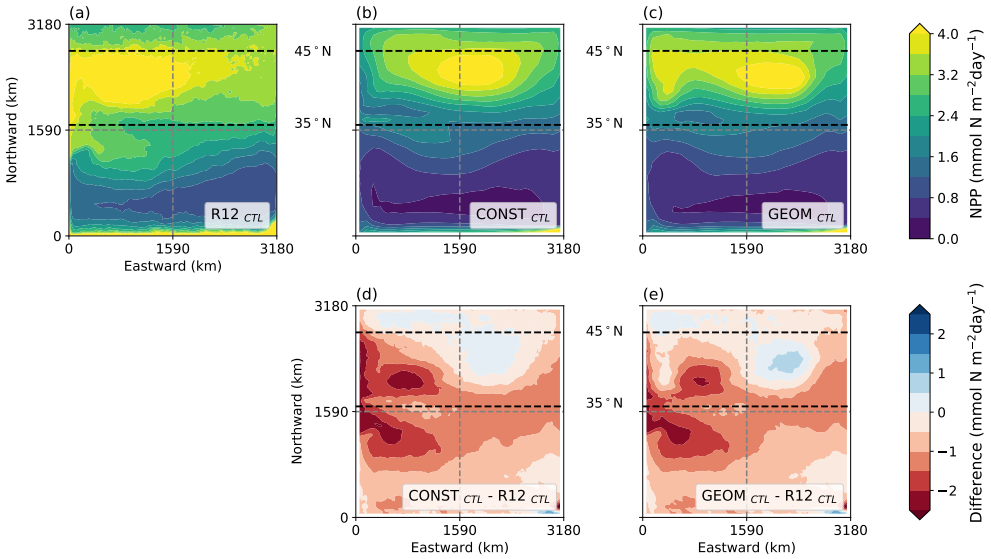

Figure 5: (Top row) Vertically integrated Net Primary Production (NPP, mmol N m^{-2} day^{-1}, where N is the nitrogen currency) for (*a*) R12, (*b*) CONST and (*c*) GEOM. (Bottom row) Raw differences with the R12 calculation for (*d*) CONST and (*e*) GEOM, where red colours denote a reduction in NPP. The area enclosed by black lines denote the subpolar box mentioned in text.

As noted in §2, the biogeochemistry model employed takes no explicit account of temperature variations on the biogeochemical activities themselves, so the changes observed are a result of the changes in the nutrient distributions. While NPP has contributions from nitrate and ammonium, as nitrate is the dominant form of dissolved inorganic nitrogen except in oxygen poor regions in the marine system (e.g. oxygen minimum zones or coastal hypoxia zones), we focus our attention on nitrate; the ratio between primary production arising from nitrate and total primary production encoded as a f-ratio (e.g., Sarmiento and Gruber, 2006, §4) is relatively constant over the set of calculations at around 0.43 (cf. Couespel et al., 2021). We show in Fig. 6 the zonally averaged vertical distribution of nitrate. In the raw values in panel *a-c* we see a suppression and elevation of nitrate concentration in the subtropical and subpolar gyres respectively across all models, consistent with the Ekman downwelling and upwelling from the choice of zonal wind forcing (e.g., §4 of Williams and Follows, 2011). In the GEOM calculation, while there is a strong decrease of nitrate concentration in the subtropical gyre possibly in line with the damped Western Boundary Current associated with the larger κ_{gm} values in the region, and an overall decrease over the whole subpolar gyre itself in panel *d*, there is an increase in nitrate concentration in the northern parts of the subpolar gyre (blue shading in panel f, and its absence in panel *e*), which collectively leads to a mildly elevated NPP in the same subpolar gyre region in GEOM as compared to CONST.

To analyse the transport properties of nitrate, we note that the advective contribution arises as $\nabla \cdot (\boldsymbol{u}N)$, where N denotes the nitrate concentration. Focusing on the subpolar gyre box, since the box zonal boundaries coincides with the zonal domain boundaries, by the divergence theorem and invoking no normal flow boundary conditions, we have

$$\int_{\mathrm{box}} \nabla \cdot (\boldsymbol{u}N)\, \mathrm{d}x\, \mathrm{d}y\, \mathrm{d}z = \left(\int_{\mathrm{south}} + \int_{\mathrm{north}} \right) vN\, \mathrm{d}x\, \mathrm{d}z + \int_{\mathrm{bottom}} wN\, \mathrm{d}x\, \mathrm{d}y. \tag{7}$$

We further consider the Reynolds decomposition

$$N = \overline{N} + N', \qquad \overline{N'} = 0 \tag{8}$$

where the overbar is still the time-average, which leads to

$$\overline{\boldsymbol{u}N} = \overline{\boldsymbol{u}}\,\overline{N} + \overline{\boldsymbol{u}'N'}, \tag{9}$$

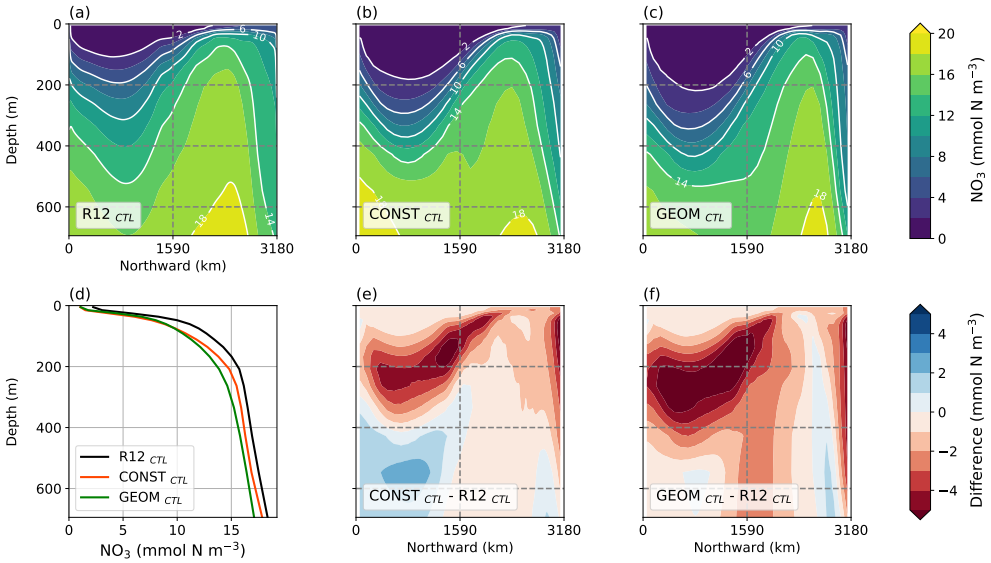

Figure 6: (Top row, a, b, c) Vertical distribution of zonally averaged nitrate concentration (NO3, mmol N m^{-3}, where N is the nitrogen currency unit), with lines of constant nitrate marked on. (Bottom row) (d) The vertical distribution of nitrate in the predefined subpolar gyre box, and (e, f) raw differences in the vertical distribution of zonally averaged nitrate with the corresponding model truth calculation, where red colours denote a reduction in nitrate concentration.

respectively the total, the mean and the eddy advective flux of nutrients, and $\boldsymbol{u}'$ is from the explicit velocity fluctuations in the case of explicit eddies, supplemented by parameterised eddy induced velocity $\boldsymbol{u}^*$ when a GM-based parameterisation is active. We compute the vertical distribution of the vertical nitrate supply, i.e.

$$\int_{y=L_s}^{y=L_n} \int_0^{L_x} \left(\overline{w}\overline{N} + \overline{w'N'} \right) \, \mathrm{d}x \, \mathrm{d}y, \tag{10}$$

where no vertical integration is implied, as well as the vertical cumulative integral of the horizontal nitrate supply at the southern and northern boundaries, i.e.

$$\int_0^z \int_0^{L_x} \left(\overline{v}\overline{N} + \overline{v'N'} \right) \, \mathrm{d}x \, \mathrm{d}\tilde{z}. \tag{11}$$

Fig. 7 shows the advective supply of nitrate and their respective vertical and meridional contributions, as well as their decompositions into the total, mean, and eddy contributions.

As expected, it is the vertical nutrient supply rate that is dominant over the top 150 m or so (Fig. 7a, b). Even though the meridional velocities are much larger than the vertical velocities, the dominance of vertical supply is expected from a geometric viewpoint, since we are dealing with small aspect ratios H/L. The vertical mixing contribution dominates over the advective contribution over the top 50 m, but is otherwise largely similar for the set of calculations (not shown here; see e.g. Couespel et al. 2021, Fig. 4). The meridional nutrient supply however becomes important with depth, since the areas associated with the meridional sections of interest are now larger, and the nutrient supply can be comparable once the differences in the typical sizes of the meridional and vertical velocities are taken into account. Starting with the model truth R12, while the meridional supply is seen as a net loss (panel b), it has also the largest vertical gain (panel a), which compensates and leads to the largest nutrient concentrations in the subpolar gyre box. The supply from the south and loss from the north (panel c, d) are both large, which is consistent with R12 having the strongest overturning circulation out of the set of calculations considered here (cf. Fig. 3). Most of the contribution to the total comes from the mean (panels e-h) rather than the eddy part (panels i-l).

For the coarse resolution calculations, roughly speaking, the GEOM calculation has a vertical and meridional nutrient supply that is closer in shape to the model truth R12, although there are notable differences in the nutrient

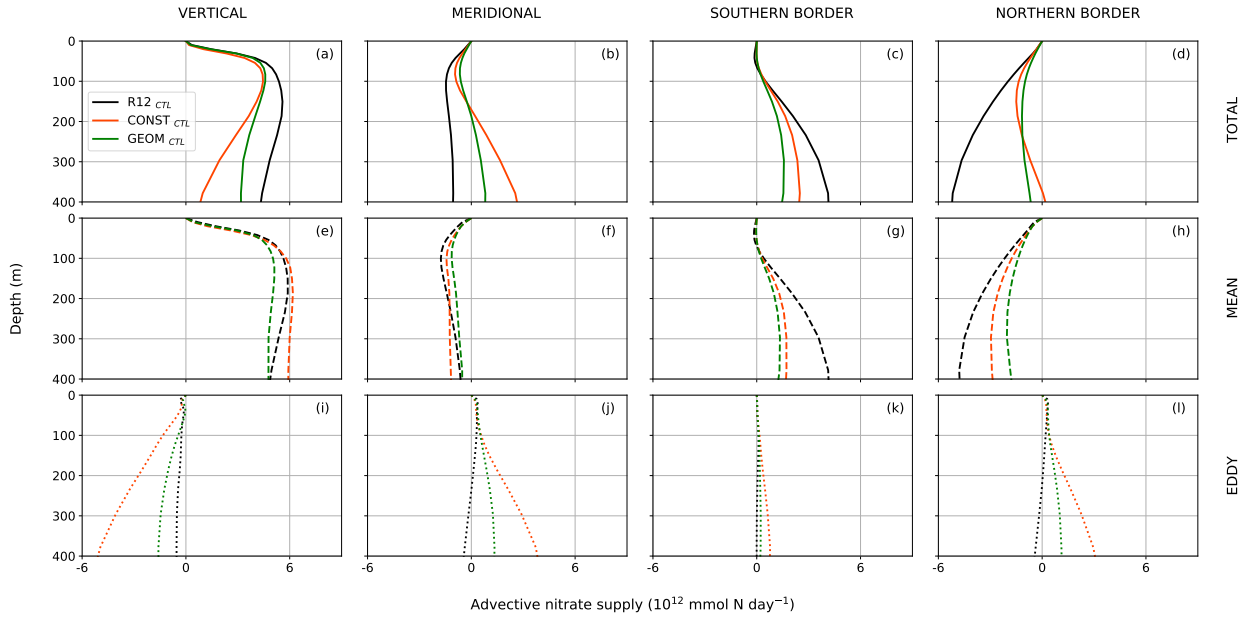

Figure 7: Advective supply of nitrate (NO3, mmol N day^{-1}, where N is the nitrogen currency unit) into the pre-defined subpolar gyre box. Shown are the vertical and meridional components (columns), as well as the total, mean and eddy advective fluxes (rows). The northern boundary contribution was calculated with an extra minus sign, so that positive values indicate a supply into the subpolar gyre box. Lateral and vertical diffusive contributions to nitrate flux are largely similar over the set of calculations and have been omitted.

supply at the southern and northern boundaries. Both CONST and GEOM have a smaller gain at the southern boundary and smaller loss at the northern boundary compared to R12, consistent with a weaker modelled overturning circulation than R12 (cf. Fig. 3). While the CONST case leads to a meridional gain of nutrients at depth, the GEOM case has a larger vertical supply (and one that is more consistent with the R12 calculation), which leads to a larger overall total supply, consistent with the diagnosed NPP values. As in the R12 case, most of the contribution is in the mean component, although the eddy part in the coarse resolution calculation (as represented by the GM scheme) is of the opposite sign and thus counteracting the mean (cf. Fig. A5 of Couespel et al. 2021), the effect being much larger in the CONST calculation. One important point to emphasise here is that while the local eddy contributions are small, it is the eddy feedback onto the mean state and the changes to the mean state that leads to the overall response that is observed (cf. Couespel et al., 2021).

One might naïvely argue that we should take κ_{gm} even smaller or even switch it off to improve the eddy component of nutrient supply and increase the NPP. Sample experiments (see Appendix A) does indeed show that the NPP *increases* with decreasing κ_{gm}, but this is at the expense of introducing un-physical deep convection into the physical response particularly along the Western Boundary Current, as mentioned near the discussion at the beginning of the section. The mean and eddy components are not isolated components that one can 'tune' separately. While the GM scheme seems to be detrimental to the local eddy component of the nutrient supply itself, it is required to have a reasonable mean state stratification and overturning circulation, with knock-on effects on the large-scale mean nutrient supply and in turn the NPP response. In that regard, the spatially varying nature of κ_{gm} afforded by GEOM allows the GM scheme on where it needs to be on for the physical response, and suppressing its effects in the subpolar gyre where it is potentially detrimental to the biogeochemical response.

A calculation with a simpler prescription of κ_{gm} based on Treguier et al. (1997) as implemneted into NEMO, which requires a specification of a maximum $\hat{\kappa}_{\mathrm{gm}}$ and varies in space according to the baroclinic growth rate) gives similar conclusions in the control calculation to GEOM. The resulting κ_{gm} is not unlike that shown in Fig. 2, but with a much more gradual spatial variation, but limited by the choice of the maximum $\hat{\kappa}_{\mathrm{gm},0}$, taken here to be 1000 m^2 s^{-1}. The resulting diagnostics are largely similar and certainly improve upon the the CONST case, for reasons detailed

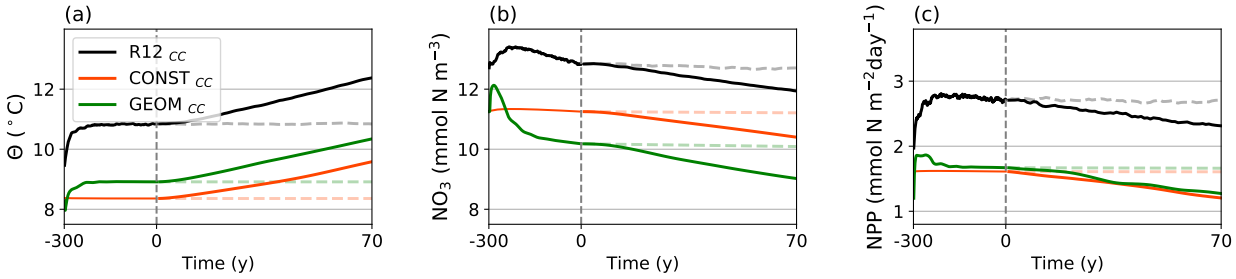

Figure 8: Time series of various quantities from the idealised climate change experiments during the analysis period (0 to 70 years), for the model truth (R12, black line) and resolution calculations (CONST, red line; GEOM, green line); the time axes are linear in the spinup and analysis period individually. (*a*) Averaged ocean temperature Θ (°C) over the top 700 m of the model domain. (*b*) Model nitrate concentration (NO3, mmol N m^{-3}, where N is the nitrogen currency unit) over the top 700 m of the model domain. (*c*) Domain integrated Net Primary Production (NPP, mmol N m^{-2} day). The corresponding dashed lines show the time series of the control runs during the same period depicted in Fig. 1(a, b, c).

already. In that regard, it is the spatially varying nature of $\kappa_{\rm gm}$ afforded by the more updated schemes that results in a modelled state that is closer to the model truth in the selected diagnostics. However, it is known that schemes with a prescribed maximum $\kappa_{\rm gm}$ tends to under-react to climate change scenarios, since we are in some sense 'fixing' the level of turbulent feedback when we might expect the eddy activity to increase under such conditions (e.g., Fox-Kemper et al., 2019). The GEOM scheme and other energetically constrained parameterisations have no such limitations, and we might expect such schemes to behave in a favourable way under the climate change scenarios.

4. Sensitivities under idealised climate change

In our idealised climate change experiments the model is exposed to the aforementioned idealised seasonal cycle from model year 0, but the imposed atmopsheric temperature is given an increasing linear trend of +0.04 °C yr^{-1} over 70 model years, following Couespel et al. (2021) to mimic the SSP5-8.5 scenario (e.g., Tokarska et al., 2020). Fig. 8 shows time-series of the average temperature, nitrate concentration and NPP under the idealised climate change scenario for the calculations. The ocean temperature increases, leading to a stronger stratification (primarily in the upper ocean; not shown) that inhibits nutrient supply and a decrease in NPP across the set of calculations.

The main interest here is in the sensitivities of the individual models to increased atmospheric temperature forcing. The model truth R12 would respond dynamically via changes in eddy characteristics in an explicit fashion, while the CONST case with its fixed and prescribed $\kappa_{\rm gm}$ coefficient in some sense has the turbulence level "fixed". On the other hand, GEOM has a dynamically varying $\kappa_{\rm gm}$ that evolves depending on the modelled mean state. Each of these cases have a local effect arising from the eddy dynamics themselves, but also a global consequence on the resulting mean state via eddy-mean interactions. A focus here is on discerning what CONST and GEOM do differently, how well they reproduce the sensitivities displayed by the model truth, and the corresponding physical and biogeochemical consequences. With that in mind, the analyses are essentially the same as in the previous section, focusing on time-averaged data during the same analysis period. Consistent with the conclusions in the last section, it will be seen here also that the spatial dependence of $\kappa_{\rm gm}$ particularly in the northern boundary is crucial for model response. Further, we find that integrated diagnostics focusing only on physical or biogeochemical responses can be somewhat misleading as it can mask out compensating erroneous effects.

4.1. Physical responses

Fig. 9 shows the resulting $\kappa_{\rm gm}$ distribution from GEOM under the climate change scenario, and the raw differences compared to the control scenario. The notable feature is the increase in $\kappa_{\rm gm}$ towards the northern boundary in panel *b* where the model deep water is formed. Given the discussion in the previous section, we would expect the GEOM calculation in this case to have an over weakened overturning circulation, which would lead to a decrease in the nutrient supply and in the NPP. Details turn out to matter, as will be seen shortly.

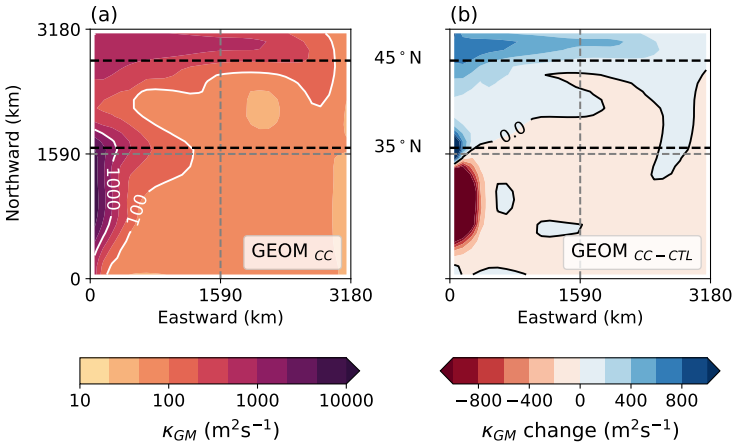

Figure 9: (*a*) The resulting κ_{gm} profile associated with GEOM under the climate change experiment, and (*b*) the raw differences of the κ_{gm} between the control and the climate change scenario (i.e. Fig. 9*a* minus Fig. 2*c*). Red colours in panel *b* indicate a decrease in κ_{gm}.

Fig. 10(a, b, c) shows the raw differences between the overturning streamfunction under climate change and the control case (cf. Fig. 3a, b, c). While both R12 and GEOM show a significant decrease in the very northern part of the domain, this feature seems to be absent in the CONST case. This lack of decrease in the overturning strength in CONST (and even a mild increase shown at the bottom right half of panel *b*) might have contributed to what is seen in Fig. 10(d, e, f) in the diagnosed northward heat transport. The R12 and GEOM calculations both show only small increases in the heat transport relative to the control scenario in the northern part of the domain (+2.04% and +5.73% increase in the area-weighted average northward heat transport north of the center of the domain for R12 and GEOM respectively), but the CONST calculation shows a rather significant increase in the heat transport in the same region (+23.5% increase in the area-weighted average northward heat transport north of the center of the domain). While the response seen in R12 and GEOM are likely because of the increase in temperature offsetting the decrease in the advective velocity, given the magnitude of the response in CONST, it is likely indicating that the overturning response under climate change scenario in CONST is inconsistent with the actual dynamics in the model truth with explicit eddies. We should thus be wary of the resulting integrated diagnostics of the biogeochemical responses for the CONST case later because of the seemingly inconsistent physical response.

Fig. 11 shows the changes in the diagnosed maximum mixed layer depth, and all panels shows that the mixed layer depth has generally shoaled across all calculations under the climate change scenario, particularly in the region near the northern boundary. This is consistent with the warming of the atmosphere and the associated decrease in buoyancy loss in the ocean experiences. However, note that the coarse resolution models appear to have a noticeably shallower mixed layer, as seen in the histograms and the median values in Fig. 11e, f compare to the R12 calculations with explicit eddies. From the preceding discussion, we might expect that the shoaling of the maximum mixed layer depth is more significant in GEOM. The statement "more shoaling" should really be interpreted in the statistical sense, suggestive from the calculated median, as well as by eye where the overall shift in the probability distributions in Fig. 11f is larger than that in Fig. 11e. We can quantify the magnitude of shifting of the probability distributions by numerically computing the 1-Wasserstein distance $W_1(\mu, \nu)$ (sometimes known as the earth mover's distance, e.g. Villani 2008) between the discrete probability distributions μ and ν. Doing so leads to $W_1(\text{GEOM}_{\text{CTL}}, \text{GEOM}_{\text{CC}}) \approx 216$ while $W_1(\text{CONST}_{\text{CTL}}, \text{CONST}_{\text{CC}}) \approx 170$ in the mixed layer depth diagnostic, thus supporting the conclusion that the GEOM calculation changes more within the climate change scenario, likely associated with the increased κ_{gm} in the northern boundary region. For completeness, $W_1(\text{R12}_{\text{CTL}}, \text{R12}_{\text{CC}}) \approx 217$, so in this metric GEOM has a sensitivity more in line with R12 than CONST.

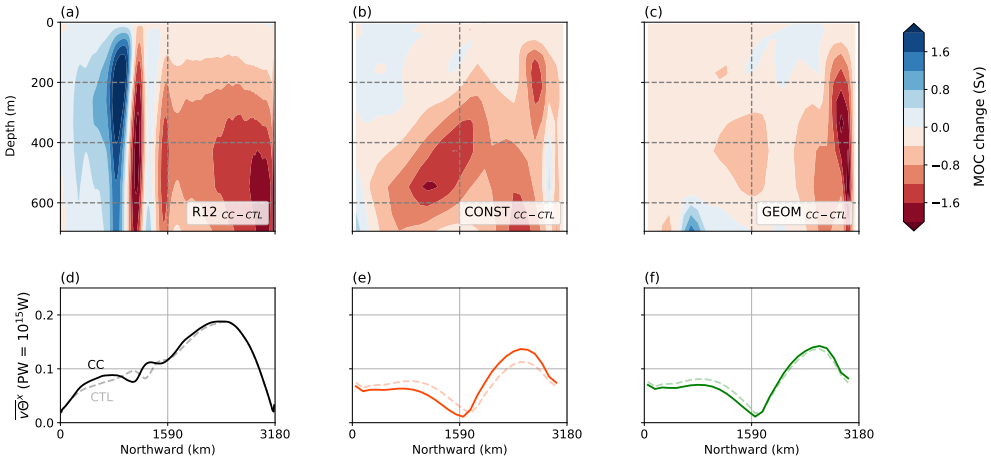

Figure 10: (Top row) Raw differences of the diagnosed overturning streamfunction Ψ_{MOC} from the climate change scenario with the corresponding control scenario (see Fig. 3, for (*a*) R12, (*b*) CONST, (*c*) GEOM; red values denote more negative values, and mostly correspond to a decrease in the overturning strength. (Bottom row) The the diagnosed northward heat transport (in units of PW = 10^{15} W) for (*d*) R12, (*e*) CONST, (*f*) GEOM under climate scenario as solid lines; the dashed line are the same quantities of the corresponding control (i.e. the lines in Fig. 3*d*).

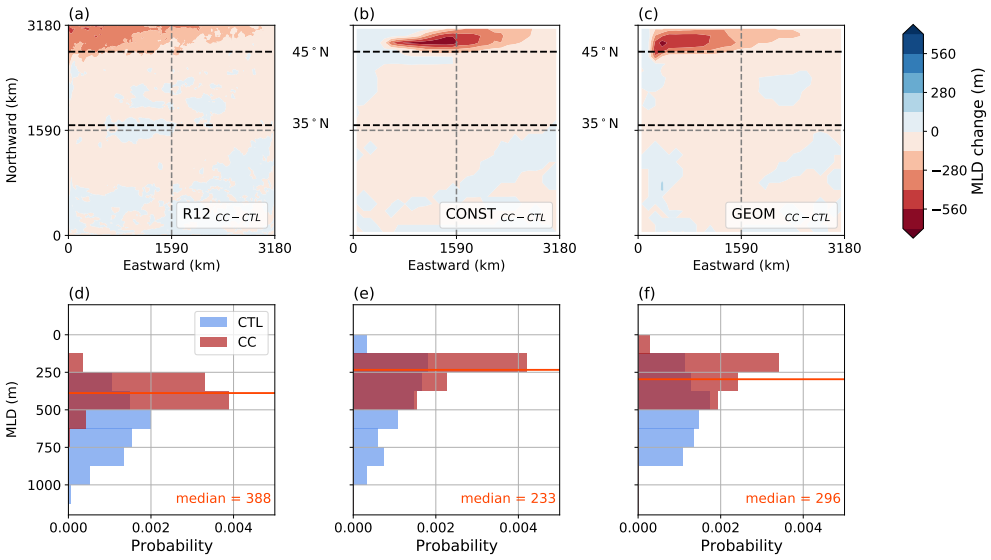

Figure 11: (Top row) Raw difference between climate change and control scenario maximum mixed layer depth (m, diagnosed as the first depth below which $|\sigma_\theta(z) - \sigma_\theta(z = -10\ \mathrm{m})| > 0.01$, where σ_θ is the potential density referenced to sea level), for (*a*) R12, (*b*) CONST and (*c*) GEOM; red colours denote a decrease in mixed layer depth (i.e. shoaling of the mixed layer). (Bottom row) Histogram of the mixed layer depth distributions and median (marked on as a line) over the subpolar gyre region of both the climate change scenario (in red) and histogram of control scenario (in blue, cf. Fig. 4*d*, *e*, *f*) for (*d*) R12, (*e*) CONST and (*f*) GEOM.

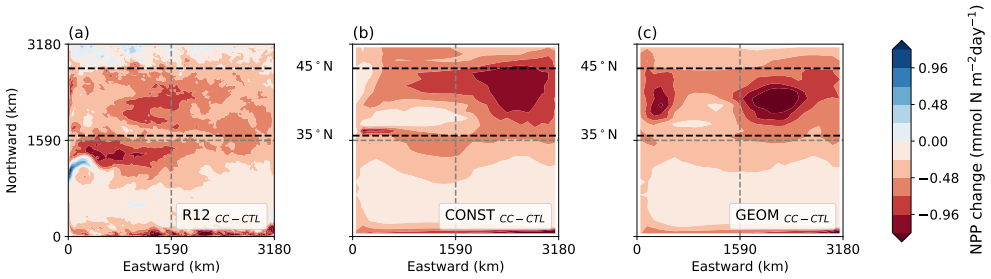

Figure 12: Raw differences of the vertically integrated Net Primary Production (NPP, mmol N m^{-2} day^{-1}, where N is the nitrogen currency) between the climate change scenario and the control scenario (Fig. 5*a*, *b*, *c*) for (*a*) R12, (*b*) CONST and (*c*) GEOM; red values denote a decrease in NPP.

4.2. Biogeochemical responses

Fig. 12 shows the raw differences in the vertically integrated NPP between the climate change and control scenarios. There is a decrease in NPP across all models under climate change particularly in the subpolar gyre, although there are isolated spots in the R12 calculation where NPP has marginally increased (south of the Western Boundary Current separation, and at the northern boundary where downwelling occurs). The decrease in NPP in the coarse resolution models are concentrated particularly in the east of the subpolar gyre region, and a small patch towards the western boundary in the GEOM calculation. Note however that these regions of strong decrease in GEOM coincide somewhat with the regions where the depth-integrated NPP was actually larger than the R12 calculation in the control scenario (see Fig. 5*d*, *e*).

The integrated NPP value averaged over the subpolar gyre declines under climate change for all calculations, with R12 at 3.16 (−13.8%), CONST at 2.13 (−22.9%) and GEOM at 2.22 (−23.6%), where the raw numbers are in units of mmol N m^{-2} day^{-1} (where N is the nitrogen currency), and the percentage difference is relative to the respective calculations in the control scenario. The R12 model simulates the largest NPP overall, with the smallest decline under the climate change scenario. The coarse resolution models significantly under predict in the raw value of the NPP, and also predict a more dramatic decline, in line with the previous results of Couespel et al. (2021). While it is true that the GEOM calculation still predicts a higher NPP than the CONST calculation in both the control and climate change scenario, the GEOM calculation displays more sensitivity to the change in forcing under the climate change scenario, with a marginally larger NPP decline relative to itself. We should however also bear in mind that there is evidence so far indicates that CONST possesses a sensitivity in the physical response that is inconsistent with the eddy resolving calculation R12 (e.g. Fig. 10), i.e. the CONST calculation might be "better" in the integrated NPP diagnostic, but not necessarily for the right reasons.

The observed decline in NPP can again be attributed to the changes in the nutrient supply. We focus our attention again on nitrate; there is a decrease in the resulting f-ratio to around 0.40 (from around 0.43) somewhat uniformly across the set of calculations. Fig. 13 shows the differences of vertical distribution of zonally averaged nitrate between the climate change and control scenario (see also Fig. 6). It is seen that there is a decline of nitrate in the upper portions of the subpolar gyre across all models, with a mild increase at depths, indicating a decline in upwelling is consistent with the strengthened stratification as indicated for example by the buoyancy frequency $N^2 \sim -\partial\rho/\partial z$ (not shown). The coarse resolution models exhibit the strongest declines, with the regions of strong decline following the changes in the mean stratification. Fig. 13*d* shows the vertical distribution of the nitrate concentration averaged over the subpolar gyre box, and it is noteworthy that the GEOM calculation has a vertical distribution that is closer to the model truth R12 than the CONST case for the present subpolar region of interest particularly in the sensitivities.

To further analyse the changes in the nutrient distribution, we perform the same decomposition of the advective fluxes of nitrate as was done in the control scenario towards the end of §3 (cf. Fig. 7). The differences in advective fluxes are shown in Fig. 14. Note that negative values in Fig. 14 largely mean a *decrease in the supply* into the subpolar gyre, while positive values mostly mean a *decrease in the loss* out of the subpolar gyre; the changes in the diffusive contributions are largely similar across the set of calculations and have been omitted. With that in mind, starting again first with the R12 case, the vertical nutrient supply decreases (panel *a*) under idealised climate change, although

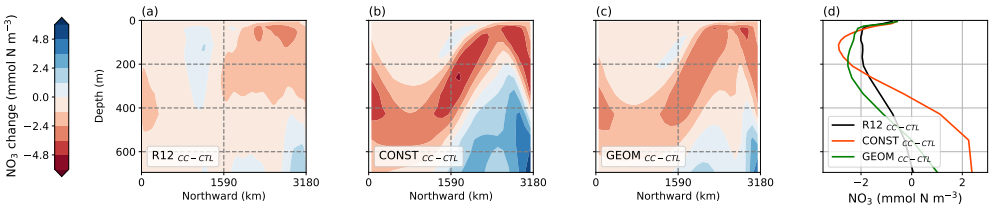

Figure 13: Raw differences between the vertical distribution of zonally averaged nitrate concentration (NO3, mmol N m^{-3}, where N is the nitrogen currency unit) between the climate change scenario and the control scenario (Fig. 6*a*, *b*, *c*) for (*a*) R12, (*b*) CONST and (*c*) GEOM; red values denote a decrease in nitrate concentration. (*d*) Raw differences in the vertical distribution of nitrate in the predefined subpolar gyre box between the climate change scenario and the control scenario (Fig. 6*d*), with negative values denoting a decrease in concentration.

the meridional loss has decreased (panel *b*). The southern boundary gain has decreased (panel *c*) while the northern boundary loss has also decreased (panel *d*), broadly consistent with a decrease in the overturning strength under the climate change scenario (cf. Fig. 10). As in the control scenario, most of the changes manifest in the mean (panels *e*-*h*) rather than in the eddy component (panels *i*-*l*).

For the coarse resolution calculations, we note that while CONST suffers a large decrease in the vertical supply (panel *a*), it seems to be compensated by an equally large decline in the total horizontal loss (panel *b*), associated with the large decrease in loss at the northern boundary (panel *d*). This is particularly interesting, given neither of these sensitivities are nearly as dramatic in the R12 calculation, and suggests that this is a case where two "wrongs" happen to cancel out, resulting in a reasonable integrated response in the NPP. On the other hand, the GEOM calculation over most panels capture the shape of the R12 responses somewhat (and arguably mostly improve on the sensitivities displayed by the CONST calculation), except at the northern boundary, and there is a notable decrease in the vertical supply in the upper 50 m of the ocean. So while the GEOM calculation seems to respond in a way that is more consistent with the model truth, it seems to (*i*) do things 'wrong' perhaps where it matters the most in the vertical nutrient supply (upper part of the ocean where light availability and NPP is the largest), and (*ii*) not have the benefit of two 'wrongs' cancelling out as in the CONST case.

5. Conclusions and discussions

Numerical ocean models at non-eddy resolving to partially eddy permitting resolutions, requiring some sort of sub-grid physics parameterisation of the mesoscale processes, are going to remain the norm for the foreseeable future. Assessment of related parameterisations to highlight the possible benefits as well as deficiencies imparted to the model by the parameterisation, are required in order to constrain our uncertainties in the relevant conclusions and projections drawn from such models. To that end, this work presents an investigation of the joint physical and biogeochemical sensitivity to the choice of mesoscale eddy parameterisation in light of the recent developments in eddy parameterisation and its improvements into the modelled physical processes. The focus here has been on the more conventional diffusive closures utilised in coarse resolution non-eddy permitting ocean models, principally on the eddy induced advection represented by the GM scheme (e.g., Gent and McWilliams, 1990; Gent et al., 1995) and the GM version of the GEOMETRIC scheme (Marshall et al., 2012; Mak et al., 2018, 2022b). The present work documents the performance of diffusive closures in coarse resolution models and the eddy resolving model truth, as a precursor to an assessment into models at eddy-permitting models as well as backscatter-type parameterisations and their impacts, to be reported elsewhere in due course.

To comprehensively assess the impacts afforded by the choice of mesoscale eddy parameterisation, this investigation employs a simplified and well-understood physical model (a double gyre configuration with a prescribed seasonal pattern leading to deep water formation near the northern boundary). Further, a simplified biogeochemistry model was chosen so as to focus on the chain of causality relating sensitivities afforded by the eddy parameterisation, its impact on the modelled state, its consequences for nutrient supply (e.g., Williams et al., 2017, 2011; Whitt and Jansen, 2020; Gupta et al., 2022) and in turn Net Primary Production (NPP). An idealised model also allows for an eddy resolving model truth that models at coarser resolutions can be compared to. The general behaviours found

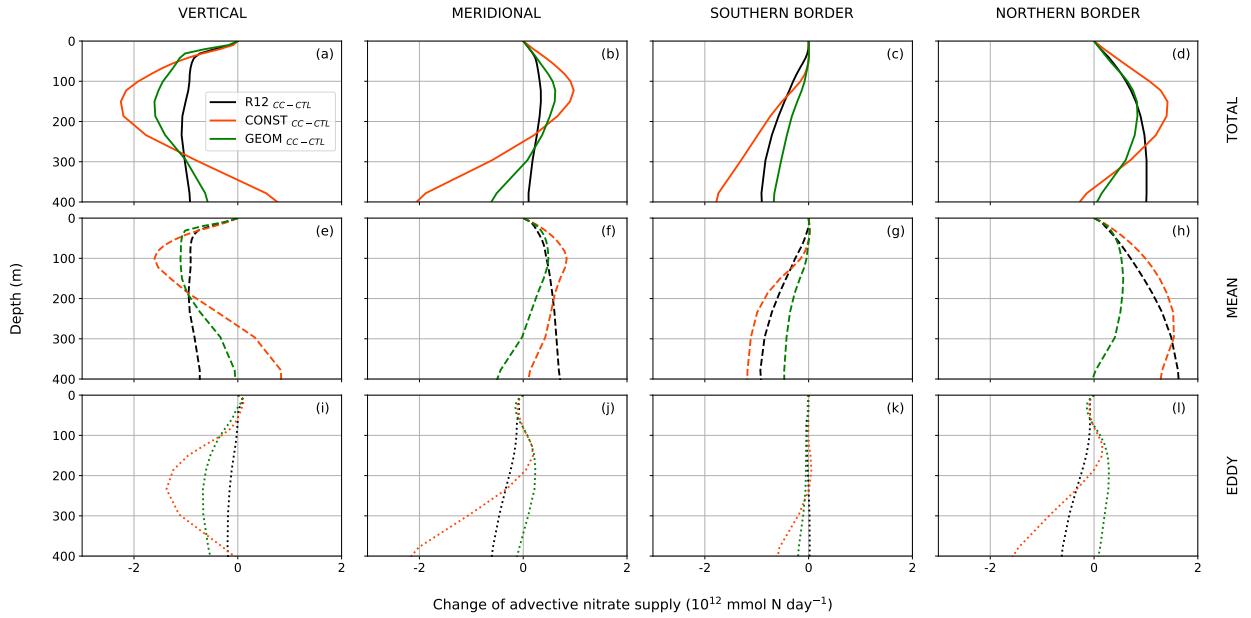

Figure 14: Differences of the advective supply of nitrate (NO3, mmol N day^{-1}, where N is the nitrogen currency unit) into the pre-defined subpolar gyre box between the climate change and control scenario (cf. Fig. 14). Shown are the vertical and meridional components (columns), as well as the total, mean and eddy advective fluxes (rows). Taking into account of the signs of the advective fluxes in Fig. 14 and the difference in magnitudes used here, negative values here largely mean a *decrease* in the supply into the subpolar gyre, while positive values mostly mean a *decrease* in the loss out of the subpolar gyre. Lateral and vertical diffusive contributions to nitrate flux are largely similar over the set of calculations and have been omitted.

are entirely consistent with that reported in Couespel et al. (2021) where, under the climate change scenario, NPP decreases, attributed to the strengthening of upper ocean stratification, leading to a weakened overturning circulation, and weakening of nutrient supply into the subpolar gyre region where the NPP is strongest. The coarse resolution models display a more significant decrease in the NPP, attributed to a weaker overturning circulation in the coarse resolution models. The previous work was all done with the standard prescription of the GM scheme, and this work extends it in the first instance by considering a more updated GM-based eddy parameterisation, as well as critically assessing the sensitivities afforded by the parameterisations and in anticipation of assessing model performance in eddy permitting models. A summary of the key diagnostics in this work and a comparison of the more updated GM-based eddy parameterisation with the constant case is given in Table 2.

The first main finding here is that the GM-version of the GEOMETRIC scheme (Marshall et al., 2012), which was found previously to lead to improved sensitivities in the modelled ocean mean state particularly when the domain includes a representation of the Southern Ocean (Mak et al., 2018, 2022b), leads to an improvement over the case where the GM coefficient $\kappa_{\rm gm}$ is set to be uniform over space, largely because the resulting $\kappa_{\rm gm}$ varies in space and is somewhat state-aware. The benefits afforded by a spatially varying $\kappa_{\rm gm}$ with reasonable properties is not entirely surprising and is somewhat known in the physical oceanography modelling community, though perhaps not so widely reported. In this particular model, the overall model response seems to be particularly sensitive to the region with deep water formation, which is consistent with theoretical considerations through the impact on the overturning circulation (e.g., Williams and Follows, 2011). Extra calculations reported in the Appendix A with prescribed spatially varying $\kappa_{\rm gm}$ further supports the reported model responses. The observed model effect is rationalised here as the eddy induced advection providing some 'resistance' just below the modelled mixed layers that resists the bending isopycnals that would result from deep water formation and associated convective events. The resulting state from using GEOMETRIC with $\kappa_{\rm gm} \sim E$ (where E is the total eddy energy) under the control scenario has a marginally stronger overturning circulation (Fig. 3), more consistent statistics in the mixed layer depths (Fig. 4), and leads to a higher nutrient supply rate and NPP (Table 2), with model characteristics that are more consistent with the model

Diagnostic	R12 values	CONST values	GEOM values	improve over CONST
overturning circulation (Sv)				
(Fig. 3a, b, c and 10a, b, c)				
L^2 mismatch rel. R12 (CTL)	—	2.29	1.99	✓
L^2 mismatch rel. R12 (CC)	—	1.87	1.63	✓
northward heat transport (10^{15} W)				
(Fig. 3d, e, f and 10d, e, f)				
area average (CTL)	0.146	0.078	0.094	✓
area average (CC)	0.148 (+2.0%)	0.097 (+23.5%)	0.099 (+5.7%)	✓ (✓)
sensitivity (L^2)	0.004	0.020	0.006	✓
northern mixed layer depth (m)				
(Fig. 4 and 11)				
median (CTL)	592	378	486	✓
median (CC)	388 (−34.5%)	234 (−38.1%)	296 (−39.1%)	✓ (×)
sensitivity (1-Wasserstein)	217	170	216	✓
NPP (mmol N m^{-2} day^{-1})				
(Fig. 5 and 12)				
area average (CTL)	3.67	2.76	2.91	✓
area average (CC)	3.16 (−13.8%)	2.13 (−22.9%)	2.22 (−23.6%)	✓ (×)
NO_3^- concentration (mmol N m^{-3})				
(Fig. 6d and 13d)				
area average (CTL)	15.61	15.57	15.01	×
area average (CC)	14.54 (−6.9%)	15.48 (−0.6%)	13.70 (−8.7%)	× (✓)
sensitivity (L^2)	1.31	2.14	1.84	✓

Table 2: Summary of diagnostics and their sensitivities for the set of calculations, where the bracketed numbers denote the percentage differences of the diagnostic between the climate change and control scenario, and L^2 denotes the area-weighted average root-mean-square difference (and has the same units as the diagnostics themselves).

truth over the CONST case. It was verified in the extra calculations with the Treguier et al. (1997) prescription of κ_{gm} (choosing maximum κ_{gm} value to be 1000 m^2 s^{-1}) leads to qualitatively similar results as GEOM in the control calculation (not shown). Without performing the calculations, we would expect similar eddy parameterisation schemes employing mixing length arguments resulting in $\kappa_{\text{gm}} \sim \sqrt{K}$ (where K is the eddy kinetic energy), such as parts of MEKE (Jansen et al., 2019), would lead to qualitative similar results as GEOM here.

The second finding, one that is more subtle, is that the GM-version of the GEOMETRIC scheme does 'worse' in the integrated NPP metric to idealised climate change compared to the standard implementation, even though the model using the GEOMETRIC scheme actually seems to mostly improve on the bulk sensitivities displayed by the model truth (e.g. nitrate concentration in Fig. 13, nutrient supply profiles in Fig. 14), and certainly more convincing and consistent than the CONST case (e.g. significant increase in heat transport in Fig. 10f, significantly different advective nutrient supply profiles in Fig. 14). The observation here seems to stem from the following: (*i*) the standard prescription of GM, while producing inconsistent sensitivities, happen to lead to cancellations (e.g. strong decrease in supply of nutrient at southern boundary in Fig. 14c and strong decrease in loss of nutrient at northern boundary in Fig. 14d), and (*ii*) the GEOMETRIC scheme happens to lead to a change in regions that lead to a particularly large impact in the model response (increase in the κ_{gm} towards the northern boundary, Fig. 9, and decrease in the vertical nutrient supply near the top of the ocean, Fig. 14a). Extra calculations (not shown) with the Treguier et al. (1997) prescription of κ_{gm} with no re-tuning leads to diagnostics that are qualitatively close to the GEOM calculations, but at a lesser magnitude, so that the integrated results are somewhat better than GEOM. The result here is likely because

the resulting $\kappa_{\rm gm}$ is still capped at the same value, thus while it is seen that the emergent $\kappa_{\rm gm}$ from the Treguier et al. (1997) prescription increases, the degree of increase is capped and thus the same influence of increasing $\kappa_{\rm gm}$ over the northern boundary region is lessened somewhat, but arguably because of the artificial limited on the parameterisation scheme. Without running the calculations, we would expect similar eddy parameterisation schemes employing mixing length arguments with $\kappa_{\rm gm} \sim \sqrt{K}$ would also do slightly better in the integrated diagnostics than GEOM because of the more muted increase in $\kappa_{\rm gm}$ over the northern boundary region.

One point to make here then is that care needs to be taken in the choice of metric to judge on the performance, and a combination of metrics might be required to highlight the intricacies of the model behaviour that are potentially masked behind a single metric, particularly when an average or integrated quantity is used. A case in hand here is that while the standard prescription of the GM scheme seems to lead to a 'better' response in integrated NPP, it is masking the fact that the contributing sensitivities are largely inconsistent with the model truth, i.e., two 'wrongs' can result in something that appears to look 'right'. Ultimately the requirement should be that the biogeochemistry response is 'better' because the underlying ocean physics is 'better', and this work highlights a cautionary example where ocean models investigating biogeochemical responses should consider the modelled physical responses where possible.

The present use of an idealised model, in addition to providing a clean investigation into the strengths and deficiencies in the parameterisation schemes, also highlights lessons that we can learn from when extending our investigation to more complex but realistic models. The idealised model here highlights that if a GM-based parameterisation scheme is to be used, some form of tapering of $\kappa_{\rm gm}$ might be required as the regions of deep water formation are approached (cf. Hallberg, 2013), since this can have knock-on effects for the overturning circulation and affect biogeochemical responses in a non-local fashion. More complex biogeochemistry models are absolutely required to assess and highlight the impact of eddy parameterisations to for example carbon and oxygen budgets (e.g., Friedlingstein et al., 2014; Berthet et al., 2019; Séférian et al., 2019; Kwiatkowski et al., 2020). Our focus here however is more process oriented, and to set out a framework for evaluating the model responses and sensitivities to parameterisation, but including more complete biogeochemistry models is definitely a possible avenue for future work.

Another choice made here is to focus on the eddy induced advection as represented by the GM scheme, sidelining the isoneutral diffusion as represented by the Redi scheme (e.g. Redi, 1982; Griffies, 1998). It is somewhat considered in the modelling community that the GM coefficient impacts the ventilation pathways via changes to the stratification profile, and in turn somewhat the rate of ventilation, while the isoneutral diffusion affects mostly the rate of ventilation (e.g., England and Rahmstorf, 1999; Matear, 2001; Gnanadesikan et al., 2015; Jones and Abernathey, 2019) without modifying the background state too much (but see Chouksey et al. 2022). A possible consequence to that view is that the theoretical developments as well as numerical assessment of the GM-based schemes are more active and mature (e.g., Eden and Greatbatch, 2008; Hofman and Morales Maqueda, 2011; Mak et al., 2018; Jansen et al., 2019; Bachman, 2019) compared to that of isoneutral diffusion (e.g., Smith and Marshall, 2009; Ferrari and Nikurashin, 2010; Abernathey et al., 2013; Groeskamp et al., 2021). With that in mind prior to our investigation, we have mostly focused on the GM-based schemes, but we did consider simulations varying the spatially constant isoneutral diffusion coefficient $\kappa_{\rm iso}$, for lack of a consensus of scheme to choose from. Our sample simulations varying the spatially constant $\kappa_{\rm iso}$ by itself seems to have very minor to negligible impacts for this setup, but there are feedback loops present if $\kappa_{\rm gm}$ is state-aware (see Appendix A). A systematic and comprehensive assessment of the isoneutral diffusion parameterisation schemes is a major undertaking, and we opted to defer a related investigation to another time.

While we would like to make use of mesoscale resolving models generally, these are still computationally prohibitive and likely to remain so for the foreseeable future. As a compromise, there is an increasing focus on eddy permitting models, to broadly refer to ocean models between around $1/2^\circ$ to $1/9^\circ$, where mesoscale eddies have an explicit but incomplete representation (e.g. the explicit eddy field is substantially less energetic, from measures such as the explicit eddy kinetic energy). As noted at the beginning of this work, existing geostrophic mesoscale eddy parameterisations largely split into diffusive closures, which was the subject of this present work, and backscatter approaches (e.g., Bachman, 2019; Jansen et al., 2019). The former are more targeted towards coarse resolution model without an explicit representation of eddies (e.g. models with around 1° horizontal resolution, such as the NEMO ORCA1 model). The latter in principle should work across models at different resolutions, but the working consensus at the time of writing seems to be that backscatter approaches work better in eddy permitting models, where backscatter parameterisations energise the eddies that are explicitly represented by the model itself. Given the increase in available computational power for performing global ocean models and Earth System Models at eddy permitting

resolutions (normally around $1/4^\circ$ horizontal resolution), and the benefits that result once ocean models go from no eddies to some eddies (e.g., Hewitt et al., 2017, 2020), an assessment into backscatter parameterisations analogous to the one carried out here is a priority, and is currently the subject of investigation.

Two fundamentally separate but in practice related queries that spring to mind are the benefits and deficiencies of (*i*) eddy permitting models themselves, and (*ii*) backscatter parameterisations, in relation to the physical as well as biogeochemical responses. Preliminary work carried out by us focusing on the former shows that while the $1/9^\circ$ models (cf., Couespel et al., 2021) are quantitatively similar to the $1/12^\circ$ model reported here, the $1/4^\circ$ model (the target resolution of next generation Earth System Models) seems to be "too good": the modelled NPP decrease is even less than the model truth under the idealised climate change scenario. This is again a case where we are getting a 'better' answer but for essentially the wrong reasons: the $1/4^\circ$ has eddies but these are too weak, resulting in the modelled mixed layer and pycnocline having a deep bias, leading to a deep overturning circulation and larger nutrient supply, with associated increase in subpolar gyre NPP. The preliminary result reinforces the cautionary point made here about integrated metrics that, while useful and easier to understand, potentially masks out important details that can be absolutely crucial. The preliminary result also suggests that the main benefits come from a model becoming eddy permitting. While this might be suggesting fundamental limitations of non-eddying models and diffusive closures, if anything the results imply we still want a bit of the diffusive behaviour associated with diffusive closures in the $1/4^\circ$ models (e.g. to counteract the deeper mixed layer and pycnocline), rather than jettison it altogether. Whether the additional diffusive behaviour should come from diffusive closures themselves explicitly, or implicitly via the backscatter approaches energising the eddies, remains an open question. This brings us back however to a long-standing question of utilising diffusive closures in such eddy permitting 'grey zone' models (e.g. Hewitt et al., 2020), since eddy permitting models by themselves under count the eddy activity, but utilising a diffusive parameterisation ends up double counting (cf., Hallberg, 2013). It is known using GM-based schemes ends up damping most of the explicit eddies permitted by the model, and makes the eddy permitting model behave more like a non-eddying model. The issue of parameterisation in eddy permitting models, on diffusive vs. backscatter-type approaches, and their separate and joint consequences on the resulting physical and biogeochemical responses is currently underway, and will be the subject of future publications.

Acknowledgements

This research was supported by Southern Marine Science and Engineering Guangdong Laboratory (Guangzhou) (SMSEGL20SC01) and the RGC General Research Fund 16304021. DC is funded under the Research Council of Norway under grant 275268 (COLUMBIA). ML acknowledges financial support from the Chanel Research Chair of ENS-PSL. The numerical model modifications, analyses code and sample model data may be found on Zenodo at `http://dx.doi.org/10.5281/zenodo.7329362`.

Appendix A. Model dependence on other parameters

Here we provide some further evidence for our assertion that the model mostly depends on $\kappa_{\rm gm}$, particularly its values around the northern boundary where deep water formation occurs, and a brief description of model dependence on other key uncertain parameters within the system, namely the GEOMETRIC parameters α and λ (see Eq. 2 and 3), and the isoneutral diffusion parameter $\kappa_{\rm iso}$.

The dynamical argument here is that the presence of $\kappa_{\rm gm}$ leads to flattening of isopycnals at the base of the mixed layer, which provides extra resistance to deep water formation by inhibiting the steepening of isopycnals that would arise. Such an effect leads to a shallow bias of the mixed layer depths, a weakening of the overturning circulation, a reduction in nutrient supply and a reduction in NPP. The argument is in line with the previous results in the Appendix of Couespel et al. (2021), as well as our own CONST experiments, where it is generally observed that the smaller the $\kappa_{\rm gm}$, the higher the NPP (for precisely the aforementioned dynamical reasons, with signatures in the mixed layer depths and other physical metrics; not shown). The highest NPP occurs for the case when the GM scheme is completely switched off, but of course at the expense of introducing un-physical deep convection around the domain, as mentioned in text.

It follows that varying the GEOM parameters α and λ affect the resulting model results in a way that is consistent with varying $\kappa_{\rm gm}$ (varying the energy diffusion coefficient η_E leads to fairly weak responses in $\kappa_{\rm gm} \sim E$

		NPP (CTL)	NPP (CC)	ΔNPP (self)
CONST	$\kappa_{\rm iso}$ = 500	2.73	2.16	−20.9%
	$\kappa_{\rm iso}$ = 1000	2.76	2.13	−22.8%
	$\kappa_{\rm iso}$ = 2000	2.87	2.22	−22.7%
GEOM	$\kappa_{\rm iso}$ = 500	2.75	2.06	−25.1%
	$\kappa_{\rm iso}$ = 1000	2.91	2.22	−23.6%
	$\kappa_{\rm iso}$ = 2000	3.11	2.48	−20.3%

Table A.3: Integrated Net Primary Production rate (NPP, mmol N m^{-2} day^{-1}, where N is the nitrogen currency) integrated over the subpolar gyre box under the climate change scenario, for various calculations with varying $\kappa_{\rm iso}$.

via modifying the sharpness of the modelled total eddy energy signature E). Increasing α and decreasing λ (or increasing the dissipation time-scale λ^{-1}) both lead to increased $\kappa_{\rm gm}$ (consistent with Mak et al. 2017; see Marshall et al. 2017 for physical rationalisation), leading to decreases in NPP again for the aforementioned reasons. While the resulting modelled state under the control scenario differ depending on the choice of GEOM parameters, the resulting sensitivities under climate change for fixed choices of α and λ are largely similar in magnitude, with a similar decrease in NPP, again because of the resulting increase in the $\kappa_{\rm gm}$ value over the northern boundary region. Although there are no strong constraints on the choice of α and λ (but see attempts in Poulsen et al. 2019 and Mak et al. 2022a), it is at least reassuring that the conclusions regarding the sensitivity under climate change scenarios are robust.

The sensitivity of the modelled state to the $\kappa_{\rm gm}$ value at the northern boundary was further supported by results from experiments where $\kappa_{\rm gm}$ was artificially enhanced/suppressed under climate change scenario, via manually modifying the CONST or GEOM $\kappa_{\rm gm}$ profiles in various regions. All results are consistent with the fact that increased $\kappa_{\rm gm}$ at the northern boundary lead to decreased NPP for the physical chain of causality detailed above. Further, the results support the notion that GEOM produces 'better' results in the control scenario because of the spatially varying $\kappa_{\rm gm}$, but is perhaps over responding somewhat under the climate change scenario, as suggested in text.

Regarding sensitivity to the isoneutral diffusion, for lack of strong evidence to suggest which prescription functions the best, we opted to study the simple case of varying the constant diffusion coefficient $\kappa_{\rm iso}$. Table A.3 documents the diagnosed NPP in the various scenarios, for both the CONST (which are results implicitly reported in the Appendix of Couespel et al. 2021) and GEOM calculations. The general conclusions here are that increasing $\kappa_{\rm iso}$ leads to increased NPP, which is consistent with the increased transport of nutrients (at least in the lateral direction in the present gyre setting), certainly in the control scenario, and is suggestive in the climate change scenario. The observed sensitivity to $\kappa_{\rm iso}$ are stronger in the GEOM case, which arises from the nonlinear state dependence of $\kappa_{\rm gm}$. In the CONST case $\kappa_{\rm gm}$ and $\kappa_{\rm iso}$ are independently prescribed, and the resulting modelled states at different $\kappa_{\rm iso}$ are not so different between the experiments at least from a qualitative point of view (and consistent with the conclusions of Couespel et al. 2021). On the other hand, in the GEOM case, increases in $\kappa_{\rm iso}$ leads to minor differences in the modelled state, which leads to changes in the calculated $\kappa_{\rm gm}$ (in this case a *decreasing* $\kappa_{\rm gm}$ over the northern boundary region, but with only very minor changes elsewhere in terms of the spatial pattern), which modifies onto the modelled state, leading to a modified $\kappa_{\rm gm}$. The claim here is that the changes in the NPP we are seeing in GEOM from changing $\kappa_{\rm iso}$ arise from a positive feedback loop through its impact on $\kappa_{\rm gm}$ and resulting changes in the modelled stratification. The present nonlinear feedback loop between $\kappa_{\rm iso}$, the modelled state and $\kappa_{\rm gm}$ arising from GEOM should be studied further, but is beyond the scope of the present work.

References

Abernathey, R., Ferreira, D., Klocker, A., 2013. Diagnostics of isopycnal mixing in a circumpolar channel. Ocean Modell. 72, 1–16.

Adcroft, A., Anderson, W., Bushuk, C. B. M., Dufour, C. O., Dunne, J. P., Griffies, S. M., Hallberg, R. W., Harrison, M. J., Held, I., Jansen, M. F., John, J., Krasting, J. P., Langenhorst, A., Legg, S., Liang, Z., McHugh, C., Radhakrishnan, A., Reichl, B. G., Rosati, T., Samuels, B. L., Shao, A., Stouffer, R., Winton, M., Wittenberg, A. T., Xiang, B., Zadeh, N., Zhang, R., 2019. The GFDL global ocean and sea ice model OM4.0: Model description and simulation features. J. Adv. Model. Earth. Syst. 11, 3167–3211.

Bachman, S. D., 2019. The GM+E closure: A framework for coupling backscatter with the Gent and McWilliams parameterization. Ocean Modell. 136, 85–106.

Bachman, S. D., Marshall, D. P., Maddison, J. R., Mak, J., 2017. Evaluation of a scalar transport coefficient based on geometric constraints. Ocean Modell. 109, 44–54.

Bates, M., Tulloch, R., Marshall, J., Ferrari, R., 2014. Rationalizing the spatial distribution of mesoscale eddy diffusivity in terms of mixing length theory. J. Phys. Oceanogr. 44, 1523–1540.
Bellomo, K., Angeloni, M., Corti, S., von Hardenberg, J., 2021. Future climate change shaped by inter-model differences in Atlantic meridional overturning circulation response. Nat. Commun. 12 (1), 1–10.
Berloff, P., 2005. On rectification of randomly forced flows. J. Mar. Res. 63, 497–527.
Berthet, S., Séférian, R., Bricaud, C., Chevallier, M., Voldoire, A., Ethé, C., 2019. Evaluation of an online grid-coarsening algorithm in a global eddy-admitting ocean biogeochemical model. J. Adv. Model. Earth Syst. 11, 1–25.
Bindoff, N. L., McDougall, T. J., 1994. Diagnosing climate change and ocean ventilation using hydrographic data. J. Phys. Oceanogr. 24 (6), 1137–1152.
Bonan, G. B., Doney, S. C., 2018. Climate, ecosystems, and planetary futures: The challenge to predict life in Earth system models. Science 359, eaam8328.
Bopp, L., Resplandy, L., Orr, J. C., Doney, S. C., Dunne, J. P., Gehlen, M., annd C. Heinze, P. H., Ilyina, T., Séférian, R., Tjiputra, J., Vichi, M., 2013. Multiple stressors of ocean ecosystems in the 21st century: projections with CMIP5 models. Biogeosciences 10, 6225–6245.
Bopp, L., Resplandy, L., Untersee, A., Le Mezo, P., Kageyama, M., 2017. Ocean (de)oxygenation from the Last Glacial Maximum to the twenty-first century: insights from Earth System models. Phil. Trans. R. Soc. A 375, 20160323.
Cessi, P., 2008. An energy-constrained parametrization of eddy buoyancy flux. J. Phys. Oceanogr. 38, 1807–1819.
Chelton, D. B., Schlax, M. G., Samelson, R. M., 2011. Global observations of nonlinear mesoscale eddies. Prog. Oceanog. 91, 167–216.
Chouksey, A., Grisel, A., Chouksey, M., Eden, C., 2022. Changes in global ocean circulation due to isopycnal diffusion. J. Phys. Oceanogr. 52, 2219–2235.
Couespel, D., Lévy, M., Bopp, L., 2021. Oceanic primary production decline halved in eddy-resolving simulations of global warming. Biogeosciences 18, 4321–4349.
Danabasoglu, G., McWilliams, J. C., Gent, P. R., 1994. The role of mesoscale tracer transports in the global ocean circulation. Science 264, 1123–1126.
de Boer, A. M., Sigman, D. M., Toggweiler, J. R., Russell, J. L., 2007. Effect of global ocean temperature change on deep ocean ventilation. Paleoceanography 22, 1–15.
Doney, S. C., Ruckelshaus, M., Duffy, J. E., J. P. Barry, F. C., English, C. A., Galindo, H. M., Grebmeier, J. M., Hollowed, A. B., Knowlton, N., Polovina, J., Rabalais, N. N., Sydeman, W. J., Talley, L. D., 2012. Climate change impacts on marine ecosystems. Ann. Rev. Mar. Sci. 4, 11–37.
Eden, C., Greatbatch, R. J., 2008. Towards a mesoscale eddy closure. Ocean Modell. 20, 223–239.
England, M. H., Rahmstorf, S., 1999. Sensitivity of ventilation rates and radiocarbon uptake to subgrid-scale mixing in ocean models. J. Phys. Oceanogr. 29, 2802–2828.
Farneti, R., Downes, S. M., Griffies, S. M., Marsland, S. J., Behrens, E., Bentsen, M., Bi, D., Biastoch, A., Böning, C. W., Bozec, A., Canuto, V. M., Chassignet, E., Danabasoglu, G., Danilov, S., Diansky, N., Drange, H., Fogli, P. G., Gusev, A., Hallberg, R. W., Howard, A., Ilicak, M., Jung, T., Kelley, M., Large, W. G., Leboissetier, A., Long, M., Lu, J., Masinam, S., Mishra, A., Navarra, A., Nurser, A. J. G., Patara, L., Samuels, B. L., Sidorenko, D., Tsujino, H., Uotila, P., Wang, Q., Yeager, S. G., 2015. An assessment of Antarctic Circumpolar Current and Southern Ocean meridional overturning circulation during 1958-2007 in a suite of interannual CORE-II simulations. Ocean Modell. 94, 84–120.
Ferrari, R., Nikurashin, M., 2010. Suppression of eddy diffusivity across jets in the southern ocean. J. Phys. Oceanogr. 40, 1501–1519.
Ferreira, D., Marshall, J., Heimbach, P., 2005. Estimating eddy stresses by fitting dynamics to observations using a residual-mean ocean circulation model and its adjoint. J. Phys. Oceanogr. 35, 1891–1910.
Fox-Kemper, B., Adcroft, A. J., Böning, C. W., Chassignet, E. P., Curchitser, E. N., Danabasoglu, G., Eden, C., England, M. H., Gerdes, R., Greatbatch, R. J., Griffies, S. M., Hallberg, R. W., Hanert, E., Heimbach, P., Hewitt, H. T., Hill, C. N., Komuro, Y., Legg, S., Le Sommer, J., Masina, S., Marsland, S. J., Penny, S. G., Qiao, F., Ringler, T. D., Treguier, A. M., Tsujino, H., Uotila, P., Yeager, S. G., 2019. Challenges and prospects in ocean circulation models. Front. Mar. Sci. 6, 65.
Friedlingstein, P., Meinshausen, M., Arora, V. K., Jones, C. D., Anav, A., Liddicoat, S. K., Knutti, R., 2014. Uncertainties in CMIP5 climate projections due to carbon cycle feedbacks. J. Climate 27, 511–526.
Gaspar, P., Grégoris, Y., Lefevre, J., 1990. A simple eddy kinetic energy model for simulations of the oceanic vertical mixing: Tests at station papa and long-term upper ocean study site. J. Geophys. Res. 95, 16179–16193.
Gent, P. R., McWilliams, J. C., 1990. Isopycnal mixing in ocean circulation models. J. Phys. Oceanogr. 20, 150–155.
Gent, P. R., Willebrand, J., McDougall, T. J., McWilliams, J. C., 1995. Parameterizing eddy-induced tracer transports in ocean circulation models. J. Phys. Oceanogr. 25, 463–474.
Gnanadesikan, A., Pradal, M., Abernathey, R., 2015. Isopycnal mixing by mesoscale eddies significantly impacts oceanic anthropogenic carbon uptake. Geophys. Res. Lett. 42 (11), 4249–4255.
Griffies, S. M., 1998. The Gent–McWilliams skew flux. J. Phys. Oceanogr. 28, 831–841.
Groeskamp, S., LaCasce, J. H., McDougall, T. J., Rogé, M., 2021. Full-depth global estimates of ocean mesoscale eddy mixing from observations and theory. Geophys. Res. Lett. 47, e2020GL089425.
Grooms, I., 2015. A computational study of turbulent kinetic energy transport in barotropic turbulence on the f-plane. Phys. Fluids 27, 101701.
Gupta, M., Williams, R. G., Lauderdale, J. M., Jahn, O., Hill, C., Dutkiewicz, S., Follows, M. J., 2022. A nutrient relay sustains subtropical ocean productivity. Proc. Natl Acad. Sci. USA 119 (41), e2206504119.
Hallberg, R., 2013. Using a resolution function to regulate parameterizations of oceanic mesoscale eddy effects. Ocean Modell. 72, 92–103.
Helm, K. P., Bindoff, N. L., Church, J. A., 2011. Observed decreases in oxygen content of the global ocean. Geophys. Res. Lett. 38.
Hewitt, H. T., Bell, M. J., Chassignet, E. P., Czaja, A., Ferreira, D., Griffies, S. M., Hyder, P., McClean, J. L., New, A. L., Roberts, M. J., 2017. Will high-resolution global ocean models benefit coupled predictions on short-range to climate timescales? Ocean Modell. 120, 120–136.
Hewitt, H. T., Fox-Kemper, B., Pearson, B., Roberts, M., Klocke, D., 2022. The small scales of the ocean may hold the key to surprises. Nat. Clim. Change 12, 496–499.
Hewitt, H. T., Roberts, M., Mathiot, P., Biastoch, A., Blockley, E., Chassignet, E. P., Fox-Kemper, B., Hyder, P., Marshall, D. P., Popova, E., Treguier, A., Zanna, L., Yool, A., Yu, Y., Beadling, R., Bell, M. J., Kuhlbrodt, T., Arsouze, T., Bellucci, A., Castruccio, F., Gan, B., Putrasahan,

D., Roberts, C. D., Van Roekel, L., Zhang, Q., 2020. Resolving and parameterising the ocean mesoscale in earth system models. Curr. Clim. Change Rep. 6, 137–152.
Hofman, M., Morales Maqueda, M. A., 2011. The response of Southern Ocean eddies to increased midlatitude westerlies: A non-eddy resolving model study. Geophys. Res. Lett. 38, L03605.
Holmes, R. M., Groeskamp, S., Stewart, K., McDougall, T. J., 2022. Sensitivity of a coarse-resolution global ocean model to spatially variable neutral diffusion. J. Adv. Model. Earth Syst. 14, e2021MS002914.
IPBES, 2019. Global assessment report on biodiversity and ecosystem services of the Intergovernmental Science-Policy Platform on Biodiversity and Ecosystem Services.
IPCC, 2019. IPCC Special Report on the Ocean and Cryosphere in a Changing Climate.
Jansen, M. F., Adcroft, A., Khani, S., Kong, H., 2019. Toward an energetically consistent, resolution aware parameterization of ocean mesoscale eddies. J. Adv. Model. Earth Syst. 1, 1–17.
Jansen, M. F., Adcroft, A. J., Hallberg, R., Held, I. M., 2015. Parameterization of eddy fluxes based on a mesoscale energy budget. Ocean Modell. 92, 28–41.
Jones, C. S., Abernathey, R. P., 2019. Isopycnal mixing controls deep ocean ventilation. Geophys. Res. Lett. 46, 13144–13151.
Jones, C. S., Cessi, P., 2016. Interbasin transport of the meridional overturning circulation. J. Phys. Oceanogr. 46, 1157–1169.
Khwatiwala, S., Graven, H., Payne, S., Heimbach, P., 2018. Changes to the air-sea Flux and distribution of radiocarbon in the ocean over the 21st century,. Geophys. Res. Lett. 45, 5617–5626.
Klocker, A., Marshall, D. P., 2014. Advection of baroclinic eddies by depth mean flow. Geophys. Res. Lett. 41, L060001.
Kwiatkowski, L., Torres, O., Bopp, L., Aumont, O., Chamberlain, M., Christian, J. R., Dunne, J. P., Gehlen, M., Ilyina, T., John, J. G., Lenton, A., Li, H., Lovenduski, N. S., Orr, J. C., Palmieri, J., Santana-Falcón, Y., Schwinger, J., Séférian, R., Stock, C. A., Tagliabue, A., Takano, Y., Tjiputra, J., Toyama, K., Tsujino, H., Watanabe, M., Yamamoto, A., Yool, A., Ziehn, T., 2020. Twenty-first century ocean warming, acidification, deoxygenation, and upper-ocean nutrient and primary production decline from cmip6 model projections. Biogeosciences 17, 3439–3470.
Lee, H., Moon, B., Jung, H., Park, J., Shim, S., La, N., Kim, A., Yum, S. S., Ha, J., Byun, Y., Sung, H. M., Lee, J., 2022. Development of the UKESM-TOPAZ Earth System Model (Version 1.0) and preliminary evaluation of its biogeochemical simulations. Asia-Pac. J. Atmos. Sci. 58 (3), 379–400.
Lévy, M., Iovlino, D., Resplandy, L., Klein, P., Madec, G., Tréguier, A., Masson, S., Takahashi, K., 2012. Large-scale impacts of submesoscale dynamics on phytoplankton: Local and remote effects. Ocean Modell. 43–44, 77–93.
Lévy, M., Klein, P., Tréguier, A., Iovino, D., Madec, G., Masson, S., Takahashi, K., 2010. Modifications of gyre circulation by sub-mesoscale physics. Ocean Modell. 34, 1–15.
Lévy, M., Visbeck, M., Naik, N., 1999. Sensitivity of primary production to different eddy parameterizations: A case study of the spring bloom development in the northwestern Mediterranean Sea. J. Mar. Res. 57 (3), 427–448.
Li, G., Cheng, L., Zhu, J., Trenberth, K. E., Mann, M. E., Abraham, J. P., 2020. Increasing ocean stratification over the past half-century. Nat. Clim. Change 10 (12), 1116–1123.
Lotze, H. K., Tittensor, D. P., Bryndum-Buchholz, A., Eddy, T. D., Cheung, W. W. L., Galbraith, E. D., Barange, M., Barrier, N., Bianchi, D., Blanchard, J. L., Bopp, L., Büchner, M., Bulman, C. M., Carozza, D. A., Christensen, V., Coll, M., Dunne, J. P., Fulton, E. A., Jennings, S., Jones, M. C., Mackinson, S., Maury, O., Niiranen, S., Oliveros-Ramos, R., Roy, T., Fernandes, J. A., Schewe, J., Shin, Y., Silva, T. A. M., Steenbeek, J., Stock, C. A., Verley, P., Volkholz, J., Walker, N. D., Worm, B., 2019. Global ensemble projections reveal trophic amplification of ocean biomass declines with climate change. Proc. Natl. Acad. Sci. USA 116 (26), 12907–12912.
Maddison, J. R., Marshall, D. P., 2013. The Eliassen–Palm flux tensor. J. Fluid Mech. 729, 69–102.
Madec, G., 2008. NEMO ocean engine. Note du Pôle de modélisation, Institut Pierre-Simon Laplace (IPSL), No. 27.
Mak, J., Avdis, A., David, T. W., Lee, H. S., Na, Y., Yan, F. E., 2022a. On constraining the mesoscale eddy energy dissipation time-scale. J. Adv. Model. Earth Syst. 14, e2022MS003223.
Mak, J., Maddison, J. R., Marshall, D. P., Munday, D. R., 2018. Implementation of a geometrically informed and energetically constrained mesoscale eddy parameterization in an ocean circulation model. J. Phys. Oceanogr. 48, 2363–2382.
Mak, J., Marshall, D. P., Maddison, J. R., Bachman, S. D., 2017. Emergent eddy saturation from an energy constrained parameterisation. Ocean Modell. 112, 125–138.
Mak, J., Marshall, D. P., Madec, G., Maddison, J. R., 2022b. Acute sensitivity of global ocean circulation and heat content to eddy energy dissipation time-scale. Geophys. Res. Lett. 49(8), e2021GL097259.
Marshall, D. P., Adcroft, A. J., 2010. Parameterization of ocean eddies: Potential vorticity mixing, energetics and Arnold's first stability theorem. Ocean Modell. 32, 1571–1578.
Marshall, D. P., Ambaum, M. H. P., Maddison, J. R., Munday, D. R., Novak, L., 2017. Eddy saturation and frictional control of the Antarctic Circumpolar Current. Geophys. Res. Lett. 44, 286–292.
Marshall, D. P., Maddison, J. R., Berloff, P. S., 2012. A framework for parameterizing eddy potential vorticity fluxes. J. Phys. Oceanogr. 42, 539–557.
Marshall, J., Adcroft, A., Hill, C., Perelman, L., Heisey, C., 1997a. A finite volume, incompressible Navier–Stokes model for studies of the ocean on parallel computers. J. Geophys. Res. 102, 5753–5766.
Marshall, J., Hill, C., Perelman, L., Adcroft, A., 1997b. Hydrostatic, quasi-hydrostatic, and non-hydrostatic ocean modelling. J. Geophys. Res. 102, 5733–5752.
Martiny, A. C., Hagstrom, G. I., DeVries, T., Letscher, R. T., Britten, G. L., Garcia, C. A., Galbraith, E., Karl, D., Levin, S. A., Lomas, M. W., Moreno, A. R., Talmy, D., Wang, W., Matsumoto, K., 2022. Marine phytoplankton resilience may moderate oligotrophic ecosystem responses and biogeochemical feedbacks to climate change. Limnol. Oceanogr. 67, S378–S389.
Matear, R. J., 2001. Effects of numerical advection schemes and eddy parameterizations on ocean ventilation and oceanic anthropogenic CO2 uptake. Ocean Modell. 3, 217–248.
Matear, R. J., Hirst, A. C., McNeil, B. I., 2000. Changes in dissolved oxygen in the Southern Ocean with climate change. Geochem. Geophys. 1 (11).

Munday, D. R., Johnson, H. L., Marshall, D. P., 2013. Eddy saturation of equilibrated circumpolar currents. J. Phys. Oceanogr. 43, 507–532.
Newsom, E., Zanna, L., Khatiwala, S., 2022. Relating patterns of added and redistributed ocean warming. J. Climate 35, 4627–4643.
Ni, Q., Zhai, X., Wang, G., Hughes, C. W., 2020a. Widespread mesoscale dipoles in the global ocean. J. Geophys. Res. Oceans 125, e2020JC016479.
Ni, Q., Zhai, X., Wang, G., Marshall, D. P., 2020b. Random movement of mesoscale eddies in the global ocean. J. Phys. Oceanogr. 50, 2341–2357.
Poulsen, M. B., Jochum, M., Maddison, J. R., Marshall, D. P., Nuterman, R., 2019. A geometric interpretation of Southern Ocean eddy form stress. J. Phys. Oceanogr. 49, 2553–2570.
Pradal, M., Gnanadesikan, A., 2014. How does the Redi parameter for mesoscale mixing impact global climate in an Earth system model? J. Adv. Model. Earth Syst. 6, 586–601.
Rahmstorf, S., 2002. Ocean circulation and climate during the past 120,000 years. Nature 419, 207–214.
Redi, M. H., 1982. Oceanic isopycnal mixing by coordinate rotation. J. Phys. Oceanogr. 12, 1154–1158.
Roberts, M. J., Jackson, L. C., Roberts, C. D., Meccia, V., Docquier, D., Koenigk, T., Ortega, P., Moreno-Chamarro, E., Bellucci, A., Coward, A. C., Drijfhout, S., Exarchou, E., Gutjahr, O., Hewitt, H., Iovino, D., Lohmann, K., Putrasahan, D., Schiemann, R., Seddon, J., Terray, L., Xu, X., Zhang, Q., Chang, P., Yeager, S. G., Castruccio, F. S., Zhang, S., Wu, L., 2020. Sensitivity of the Atlantic Meridional Overturning Circulation to model resolution in CMIP6 HighResMIP simulations and implications for future changes. J. Adv. Model. Earth Sys. 12, e2019MS002014.
Sarmiento, J. L., Gruber, N., 2006. Ocean Biogeochemical Dynamics. Princeton University Press.
Séférian, R., Nabat, P., Michou, M., Saint-Martin, D., Voldoire, A., Colin, J., Decharme, B., Delire, C., Berthet, S., Chevallier, M., Sénési, S., Franchisteguy, L., Vial, J., Mallet, M., Joetzjer, E., Geoffroy, O., Guérémy, J., Moine, M., Msadek, R., Ribes, A., Rocher, M., Roehrig, R., Salas-y-Mélia, D., Sanchez, E., Terray, L., Valcke, S., Waldman, R., Aumont, O., Bopp, L., Deshayes, J., Éthé, C., Madec, G., 2019. Evaluation of CNRM Earth System Model, CNRM-ESM2-1: Role of Earth system processes in present-day and future climate. J. Adv. Model. Earth. Syst. 11 (12), 4182–4227.
Smith, K. S., Marshall, J., 2009. Evidence for enhanced eddy mixing at middepth in the Southern Ocean. J. Phys. Oceanogr. 39, 50–69.
Swearer, S. E., Treml, E. A., Shima, J. S., 2019. A review of biophysical models of marine larval dispersal. CRC Press.
Tagliabue, A., Kwiatkowski, L., Bopp, L., Butenschön, M., Cheung, W., Lengaigne, M., Vialard, J., 2021. Persistent uncertainties in ocean net primary production climate change projections at regional scales raise challenges for assessing impacts on ecosystem services. Front. Clim. 3, 738224.
Takano, Y., Ito, T., Deutsch, C., 2018. Projected centennial oxygen trends and their attribution to distinct ocean climate forcings. Global Biogeochem. Cycles 32, 1329–1349.
Tokarska, K. B., Stolpe, M. B., Sippel, S., Fischer, E. M., Smith, C. J., Lehner, F., Knutti, R., 2020. Past warming trend constrains future warming in CMIP6 models. Sci. Adv. 6, eaaz9549.
Treguier, A. M., Held, I. M., Larichev, V. D., 1997. Parameterization of quasigeostrophic eddies in primitive equation ocean models. J. Phys. Oceanogr. 27, 567–580.
Tschumi, T., Joos, F., Gehlen, M., Heinze, C., 2011. Deep ocean ventilation, carbon isotopes, marine sedimentation and the deglacial CO_2 rise. Clim. Past. 7 (3), 771–800.
Vallis, G. K., 2006. Atmospheric and Oceanic Fluid Dynamics. Cambridge University Press.
Villani, C., 2008. Optimal Transport: Old and New. Springer.
Visbeck, M., Marshall, J., Haine, T., Spall, M., 1997. Specification of eddy transfer coefficients in coarse-resolution ocean circulation models. J. Phys. Oceanogr. 27, 381–402.
Wang, Q., Danilov, S., Sidorenko, D., Timmermann, R., Wekerle, C., Wang, X., Jung, T., Schröter, J. G., 2014. The Finite Element Sea Ice-Ocean Model (FESOM) v.1.4: formulation of an ocean general circulation model. Geosci. Model Dev. 7, 663–693.
Wang, Y., Stewart, A. L., 2020. Scalings for eddy buoyancy transfer across continental slopes under retrograde winds. Ocean Modell. 147, 101579.
Waterman, S., Hogg, N. G., Jayne, S. R., 2011. Eddy-mean flow interaction in the Kuroshio extension region. J. Phys. Oceanogr. 41, 1182–1208.
Waterman, S., Hoskins, B. J., 2013. Eddy shape, orientation, propagation, and mean flow feedback in western boundary current jets. J. Phys. Oceanogr. 43, 1666–1690.
Waterman, S., Jayne, S. R., 2012. Eddy-driven recirculations from a localized transient forcing. J. Phys. Oceanogr. 42, 430–447.
Waterman, S., Lilly, J. M., 2015. Geometric decomposition of eddy feedbacks in barotropic systems. J. Phys. Oceanogr. 45, 1009–1024.
Wei, H., Wang, Y., Stewart, A. L., Mak, J., 2022. Scalings for eddy buoyancy fluxes across prograde shelf/slope fronts. submitted to J. Adv. Model. Earth. Syst.
Whitt, D. B., Jansen, M. F., 2020. Slower nutrient stream suppresses Subarctic Atlantic Ocean biological productivity in global warming. Proc. Natl. Acad. Sci. USA 117, 15504–15510.
Williams, R. G., Follows, M. J., 2011. Ocean Dynamics and the Carbon Cycle: Principles and Mechanisms. Cambridge University Press.
Williams, R. G., McDonagh, E., Roussenov, V. M., Torres-Valdes, S., Kind, B., Sanders, R., Hansell, D. A., 2011. Nutrient streams in the North Atlantic: Advective pathways of inorganic and dissolved organic nutrients. Global Biogeochem. Cycles 25, GB4008.
Williams, R. G., Roussenov, V. M., Follows, M. J., 2017. Nutrient streams and their induction into the mixed layer. Global Biogeochem. Cycles 20, GB1016.
Zanna, L., Khatiwala, S., Gregory, J. M., Ison, J., Heimbach, P., 2019. Global reconstruction of historical ocean heat storage and transport. Proc. Natl. Acad. Sci. USA 116, 1126–1131.
Zhang, Y., Vallis, G. K., 2013. Ocean heat uptake in eddying and non-eddying ocean circulation models in a warming climate. J. Phys. Oceanogr. 43, 2211–2229.